공학석사 학위 논문

DEVELOPMENT OF RADIO-FREQUENCY GENERATOR (RFG) SYSTEM AND PLASMA CHARACTERISTICS INVESTIGATION OF RADIO-FREQUENCY ION THRUSTER

울산대학교 대학원

기계공학과 항공우주공학전공

VU HOAI DUC

Development of Radio-Frequency Generator (RFG) system and Plasma characteristics investigation of Radio-Frequency Ion Thruster

Author: **Vu Hoai Duc**

Advisor: **Professor Shin Jichul**

THESIS

Presented to the Faculty of the Graduate School of University of Ulsan

In Partial Fulfillment of the Requirement for the Degree of

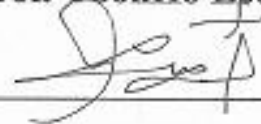Master of Science in Aerospace Engineering

University of Ulsan

2021

DEVELOPMENT OF RADIO-FREQUENCY GENERATOR (RFG) SYSTEM AND PLASMA CHARACTERISTICS INVESTIGATION OF RADIO-FREQUENCY ION THRUSTER

This certifies that the dissertation of

VU HOAI DUC is approved by

Committee Chairman: Prof. YoonHo Lee

Committee Member: Prof. SangJo Choi

Committee Member: Prof. JiChul Shin

Department of Aerospace Engineering

University of Ulsan, Korea

December 2021

Acknowledgement

First and foremost, I want to express my gratitude to my advisor, Professor Jichul Shin for his great support and guidance throughout the project. His insightful advice and feedback have improved my thinking and helped to make this thesis possible. Thank you for teaching me many important things in the research ways and making my time in South Korea enjoyable. I would like to thank my thesis defense committee members, Professor Choi Sang Jo and Professor Young Ho Lee for their perceptive and valuable comments that could improve my research topic significantly. I would also like to thank my colleagues at AARL. Your help and collaboration have been very supportive and thoughtful, and it has been a wonderful time working with all of you. I would like to appreciate the dedication of the professors and staff at the University of Ulsan. Your teachings and supports have been always helpful and it makes my study and research experience pleasurable. Finally, I would like to show my utmost appreciation to my families and friends, who have always been standing by my side through everything in this wondrous journey

Abstract

In this thesis, the development of a radio frequency (RF) power supply system for the small type of radio frequency ion thruster and the investigation of plasma impedance inside the discharge chamber are presented. This is a section in the project of developing the entire 50W laboratory model RF ion thruster at the University of Ulsan. The RF ion thrusters inductively coupled plasmas characteristics were investigated by a 0-D discharge chamber analytical model and a 2D axisymmetric numerical simulation. The RF power supply was designed by utilizing class E RF power amplifier topology for high efficiency of power conversion from DC to RF power and impedance matching network for maximum power transfer to plasmas. The RF power amplifier was theoretically analyzed and designed, simulated with a circuit simulation program to design and optimize the performance. The impedance matching network uses the plasma investigation results to approximate the load in the RF ion thruster and design a matched circuit utilizing tunable components. The RF power supply was tested with dummy load and proved to provide stable RF output waveform stably and achieve a high-power conversion efficiency of up to 85%. The simulation of plasmas inside the discharge chamber delivered important information about the characteristics of plasmas that could help to understand and have a better design of RF power supply like plasma density and absorbed power.

The RF power system is developed for the small RF ion thruster laboratory model and tested in this model to verify the calculations. This concept could be utilized to develop a larger system with high power and frequency as the efficiency could be increased with better thermal solutions. Plasma analysis using an analytical model and numerical simulation gives a deep insight into the RF ion thruster operating load and assist in the design of the impedance matching network. The tunable matching network concept was digitally controlled which could enhance the matching time, hence increase the total electrical efficiency of the system. Testing of the RF power system in the vacuum chamber has proved the ability to generate plasma of the power system.

Contents

List of Figures

List of Tables

1 Introduction

1.1 Introduction to electric space propulsion and RF power supply system

Electric space propulsion is a technology utilizing electrical and feasibly magnetic fields to accelerate or decelerate the velocity of a spacecraft. Most types of electrically powered propulsion are capable of achieving thrust with high exhaust velocities [1], thus gain the advantages of propellant reduction and higher lifetime than other propulsion methods. The thrust of electric propulsions is much weaker than that of chemical rockets but can be operated in a long time thanks to the significantly reduced propellant mass. Therefore, electric propulsion is suitable for terrestrial missions such as orbit maneuvering[2], attitude control of satellites, deep space probe, exploration, and deep space robotic vehicles application[3].

The history of electric propulsion dates back to 1906 with the idea thought of by Robert H. Goddard in [4]. Several concepts of electric propulsion were then devised and comprised in 1949 by Shepherd and Cleaver. It was not until 1964 that the first electric propulsion was operated for 30 minutes in space[5]. During the following decades to the present, many types of electric propulsion were conceived and tested in laboratories as well as in space missions. According to the literature [1], the electric propulsion common types could be divided into the following categories by their means of acceleration to produce thrust. Those types are presented in Table 1.1 below.

Table 1.1: Typical type of electric propulsions

Means of acceleration	Electric propulsion
Electrothermal	Resistor jet
	Arc jet
Electrostatic	Ion Thruster
Electromagnetic	Hall Thruster
	Electrospray/Field Emission Electric Propulsion
	Pulsed Plasma Thruster
	Magnetoplasmadynamic (MPD) Thruster

In the electric propulsion family, ion thruster is introduced to have the highest efficiency (60% to 80%) and very high specific impulse (over 10000s) [1]. This type of propulsion utilizes various type of

plasma generation method to ionize propellant. Ionized ions are extracted and accelerated by a high voltage biased grids system with multiple apertures to generate thrust. By plasma generation methods, ion thruster could be divided into three different types: DC ion thruster, RF ion thruster, and microwave ion thruster. The first type employs a DC electron-discharge plasma that uses an electron source (hollow cathode) and a magnetically enhanced discharge chamber to confine the plasma. The RF and microwave ion thruster utilize high-frequency induction heating to generate inductively coupled plasma. This alternative is preferred as it terminates the sputtering erosion of electrodes, hence increase the lifetime of the thruster. However, RF ion thruster can only work under certain conditions: propagating wave must be at the right frequency so that the reflected could be removed, the power coupled must be sufficient for induction heating and sustenance of plasma... Thus, the development of the RF ion thruster could be complicated compared to other types of plasma thrusters. Since 1962, RF ion thrusters had been developed at the University of Giessen in Germany. The RIT family was developed and scaled up to 50 cm in diameter and 120kW power and has become a standard for RF ion thruster development [6]. Many improvements have been accomplished such as scaling up for large spacecraft or down for miniature ones, utilizing many types of propellant (Argon, Xenon, Iodine...), improved ion optics design... Various RF ion thrusters have been operated in space mission could be named: RIT-10 in ARTEMIS (Advanced Relay and Technology Mission Satellite) spacecraft (Figure 1.1 [7], Iodine BIT-3 of Busek in "Luna IceCube" and "LunaH0Map" 6U CubeSats on NASA's SLS EM-1 (Figure 1.2) [8].

Figure 1.1 Artemis with electric propulsions system [ESA]

Figure 1.2 Prototype BIT-3 Thruster firing on iodine.

An example of an RF ion thruster system is presented in Figure 1.1. In an RF ion thruster system, there are several peripheral sub-systems, including gas supply, RF power supply, grids power supply, neutralizer. The propellant, usually xenon or argon, supplied by the gas feeding system, flows to the discharge chamber through a flow controller with a specific flow rate. Here, it is ionized by induction heating of the RF power supplied to an antenna (usually in helical coil shape) swathed around the discharge chamber. The heavy ions are extracted and accelerated by the grid system and form the output plume of the thruster.
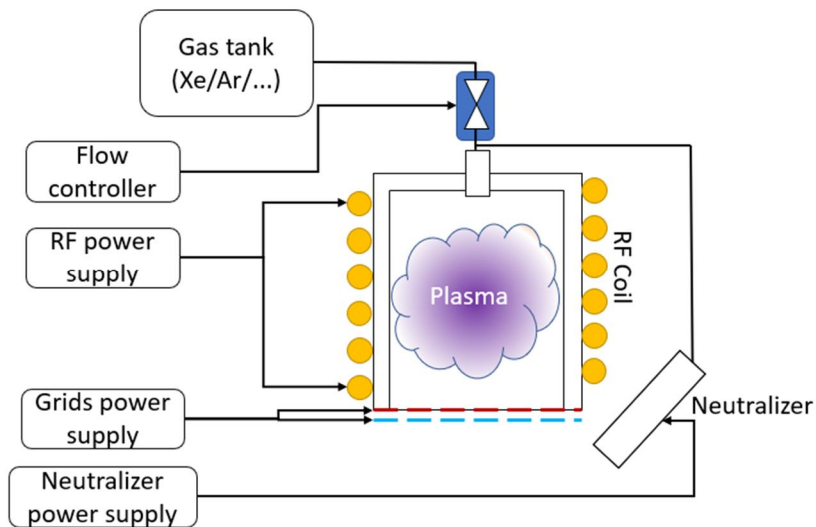
Figure 1.3 Typical RF ion thruster system

In the power supply system, the RF power supply could be considered as one of the most important sub-systems. It is the heart of the RF ion thruster which generates and sustains plasma inside the

discharge chamber. RF power supply was structured from RF power amplifier and RF impedance matching network, disciplines of RF power electronics.

RF power electronics has seen rapid growth in the last few decades with the rise of the semiconductor electronics manufacturing industry. In 2010, for each person living on Earth, more than a billion transistors were produced [9]. In the RF power amplifier field, there are several different modes called "classes". These classes are classified based on their operating modes and design goals. Some with the names class A, class AB, class B, class C are linear classes and are usually used in the audio power amplifier. These classes are differentiated by the conduction angle of the drain/collector current as in Figure 1.4. The others, namely class D, class E, class DE, class F are switch-mode amplifier which utilizing the transistor as a switch. These classes are used more frequently in industrial applications and space propulsion applications also. The switch-mode RF power amplifiers found in RF ion thruster are usually class D [10], [11], or class E [12], [13]. Table 1.2 shows a comparison between different types of RF power amplifiers.
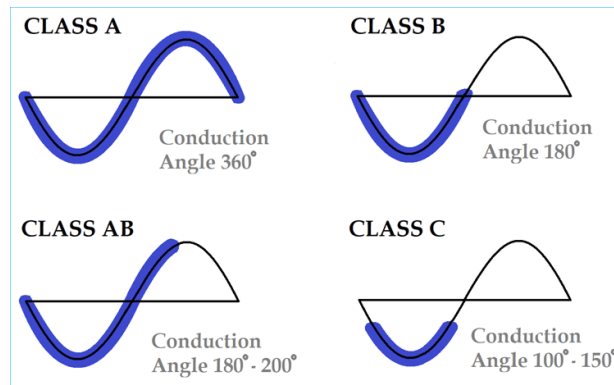
Figure 1.4 Linear classes of RF power amplifiers

Table 1.2 Comparison between different type of RF power amplifiers

Class	Type	Linearity	Power Efficiency	Ease of implementation	Power capability
A	Non-switching	Excellent	Poor	Very good	Low
B	Non-switching	Medium	Good	Very good	High
AB	Non-switching	Good	Fair	Good	Medium/High
C	Non-switching	Poor	Good	Fair	High
D	Switch-mode	Poor	Very good	Very good	High
E	Switch-mode	Poor	Excellent	Good	High
F	Switch-mode	Poor	Excellent	Fair	High

1.2 Thesis scope and outline

This thesis will be focused on these aspects of RF power supply system design for RF ion thrusters: RF ion thruster plasma impedance model: analytical and simulation, RF power amplifier circuit design, analysis and simulation, RF impedance matching circuit model design, electrical measurement of the RF power supply system with the iU-50 RF ion thruster in laboratory operation. RF plasma impedance model was analyzed based on a previously developed 0-D analytical model at the University of Ulsan [14] as well as a 2-D axisymmetric particle-in-cell (PIC) coupled with Monte Carlo collision (MCC) plasma model at the discharge chamber. Circuit design and simulation were carried out in a Simulation Program with Integrated Circuit Emphasis (SPICE) software. Detail subjects in each following chapter are as below:

Chapter 2 will present theoretical and background information covered in this thesis. The fundamentals of space propulsion will be discussed. Next, the information about the iU-50 RF ion thruster laboratory model at the University of Ulsan will be described in detail: structures, dimension, and operation. A short overview of inductively coupled plasma physics will also be covered in this part. Finally, the proposed RF power supply system will be described briefly with the essentials of RF power amplifier and RF impedance matching network.

Chapter 3 will describe the plasma impedance model in a discharge chamber and calculate the practical value used for the impedance matching circuit. An ICP discharge transformer model will be introduced. The 0-D analytical model for the iU-50 RF ion thruster laboratory model will be reviewed, analyzed, and extracted required data for the transformer model. The data extracted will be put into calculations of the transformer model of the plasma and verified with a 2-D plasma simulation in commercial plasma modeling software.

Chapter 4 will discuss the circuit design process as well as simulation results. It will cover both those parts of the RF power amplifier and RF impedance matching network. Theoretical design and calculation for a Class E power amplifier were conducted and optimum values for practical circuit fabrication were selected with the help of the simulation process. The values were satisfied, and a prototype circuit was built for testing purposes. RF impedance matching circuit was also designed and fabricated based on the approximation calculated in chapter 3.

Chapter 5 is the recaps of prototype circuit performance with power measurements and plasma generation ability in RF ion thruster experiments. Stable and high-efficiency tests of the prototype circuit have been recorded for further evaluation.

The final chapter, chapter 6 concludes the thesis and contains future suggestions for further developments of the system.

2 Theoretical Background

2.1 Fundamental of electric space propulsion

Transportation has been always an essential part of the development history of mankind. Since the dawn of man, civilizations with early mounted animals' domestication had seen the most prosperous eras. Then comes the invention of the wheel, sailing, steam engines, motors... which have been walking along throughout human history. Modern history to the present has seen rocket and space propulsion as the revolutionary in transportation, a key to the space exploration era. The year 2020 had witnessed numerous in-space rocket launches. Some significant spaceflights could be named: SpaceX's Dragon 2 spacecraft carried by Falcon 9 rocket (Figure 2.1), Starlink satellite launch at low Earth orbit... Human has landed on the moon and been aiming for the Mars and beyond. Along with that, space propulsions will be the essential technology for this ambitious goal.

Figure 2.1 Falcon 9 lifts off (http://spacex.com)

The rocket history dated back to the tenth century in China with the invention of gunpowder propelled rocket arrows by Feng Jisheng and Yue Yifang [15]. In the feudal period of history, rocket technology was used mainly as a tool of war or entertainment. In the nineteenth and early twentieth century, the rocket pioneers, namely Goddard, Oberth, von Braun, Tsiolkovsky, Korolev had built up the foundations for rocket and space propulsion technology both theoretically and experimentally [16]. In the cold war period, the Soviet space program had outdone its opponents in the space race as well as

in space history with many achievements: the first artificial satellite (the Sputnik 1), the first man in space (Yuri Gagarin), the first space station (the Salyut 1). The U.S had replied with their first human landed on the moon (Neil Armstrong) and the 84-day human-crewed space record. Nowadays, there are active space and launcher programs all over the world, not just in superpower countries. Space exploration has become an era-changing goal for all mankind.

2.1.1 The rocket equation

A rocket is a device that propels itself by emitting a jet of matter [16]. The force which projects the exhaust is also the force that thrusts the rocket. This is stated in Newton's third law of motion: "For every action, there is an equal and opposite reaction". The force accelerating the rocket is formulated as:

$$F = T = -\frac{d}{dt}\left(m_p v_{ex}\right) = -\frac{v_{ex} dm_p}{dt}$$
(2.1)

where m_p is the mass of the propellant and v_{ex} is the effective exhaust velocity. For motion in a straight line, this equation can be derived and solved for the velocity at the final time as:

$$v_i - v_f = \Delta v = v_{ex} \, ln\left(\frac{m_d}{m_d + m_p}\right)$$
(2.2)

Or we can rewrite it as:

$$m_d = \left(m_d + m_p\right)e^{\frac{\Delta v}{v_{ex}}}$$
(2.3)

where m_d is the delivered mass of the rocket and v_i, v_f are the initial and final velocities, respectively. The relationship showing in the above equation indicates that the propellant mass increases exponentially with the Δv. Thruster with high exhaust velocity over required velocity difference will have a propellant mass equals to only a little fraction of the initial mass of spacecraft.

The exhaust velocity of chemical rockets is limited with typical values up to 4 km/s. However, in electric propulsions, the propellant is unconnected from the power source, thus not subject to the limitation of the energy of the chemical bond like in the chemical kind. Modern ion and Hall thrusters with xenon as propellant could have exhaust velocity from $20 - 40$ km/s and $10 - 20$ km/s, respectively [1]. Electric propulsions are characterized by these properties: Thrust, Specific Impulse, Efficiency.

2.1.2 Thrust

Thrust is one of the characteristics of a thrusters. It is the force that propels the spacecraft and is supplied by the engine. The formula for thrust in space propulsion can be expressed as:

$$T = \frac{d}{dt}\left(m_p v_{ex}\right) = \dot{m}_p v_{ex}$$
(2.4)

where $\dot{m}_p$ is the mass flow rate of the propellant since the mass changes with time because of the consumption of the propellant. For electric propulsion types like Hall or ion thrusters, the exhaust velocity is the velocity of ions accelerated by electrical power. The ion exhaust velocity is given by:

$$v_i = \sqrt{\frac{2qV_b}{M}} \qquad (2.5)$$

where V_b is the total voltage across that ion was accelerated through, q is the charge and M is the ion mass. The mass flow rate of ion is related to the ion current beam, given by:

$$\dot{m}_\iota = \frac{I_b M}{q} \qquad (2.6)$$

Finally, we obtain the equation of thrust for unidirectional, singly ionized, monoenergetic beams of ion type of the electric propulsion is:

$$T = \sqrt{\frac{2M}{e}} \, I_b \sqrt{V_b} \qquad (2.7)$$

However, the beam of an electric thruster usually got diverged. The total corrected thrust with the term of thrust correction $\gamma = \alpha F_t$ is:

$$T = \gamma \sqrt{\frac{2M}{e}} \, I_b \sqrt{V_b} \qquad (2.8)$$

2.1.3 Specific Impulse

Specific impulse or Isp for short is the thrust efficiency measurement which is determined by the thrust over the rate of propellant consumption. It is formulated by:

$$Isp = \frac{T}{\dot{m}_p g} \qquad (2.9)$$

where $g = 9.807 \, m/s^2$ is the gravity acceleration. Specific impulse has the unit of second.

A thruster with a higher specific impulse will use the propellant mass more efficiently. A propulsion system having high specific impulses could use higher energy. A power versus specific impulse for Electric propulsion systems chart from [17] is shown in Figure 2.1. High Isp type of electric propulsion such as ion and Hall thruster has a trend of consuming more power.
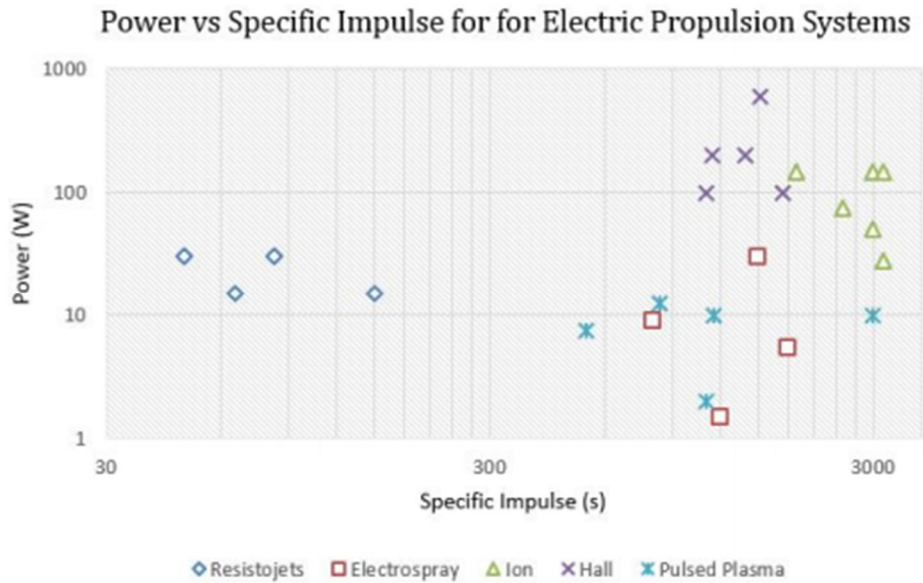
Figure 2.2 Power vs. Specific Impulse for Electric Propulsion Systems

2.1.4 Thruster efficiency

Mass utilization efficiency of an electric thruster is defined by the proportion of the propellant ionized into ions and electrons over the total input propellant.

The electrical efficiency of an electric thruster is the output beam power over the input power and is given by:

$$\eta_E = \frac{P_b}{P_I} \qquad (2.10)$$

where P_b is the beam power, P_I is the total input power include the beam power and others: electrical to produce and sustain the plasma, grids power...

The ion production efficiency is defined as the ratio of power to produce the ions over the current ion produced and formulated as:

$$\eta_d = \frac{P_d}{I_b} \qquad (2.11)$$

This efficiency is commonly called discharge loss and has the units of watts per ampere (W/A) or electron-volts per ion (eV/ion). It is ideal to have discharge loss be as small as possible. The performance of an electric thruster is usually visualized by charting the discharge loss versus the mass utilization efficiency.

2.2 RF power supply system in RF ion thruster

2.2.1 RF ion thruster descriptions

The structure of an RF ion thruster is briefly introduced in chapter 1 and it will be investigated more thoroughly in this part. In Figure 2.3, the operation of a typical RF ion thruster is presented. The input propellant, usually neutral gas (Argon, Xenon, or Iodine) is injected into a discharge chamber through a flow rate controller to manipulate and monitor parameters. The discharge chamber can vary in shape (cylindrical, conical, hemispherical) and size (few millimeters to hundreds of centimeters). It is usually made of insulating ceramic alumina or quartz materials. Wrapping around the discharge chamber is an RF coil, which could be modeled as a solenoid with N turns. The RF voltage is applied to drive an RF current through the coil. In general, RF frequencies are selected followed by the size of the discharge chamber, specifically the beam diameter by the scaling law developed in [18]. At the appropriate frequency, the coil current induces an electromagnetic field. This also induces RF current in the plasma and transfer energy to inside electrons, controls the plasma density. Neutral gas is ionized to ions and electrons and plasma is sustained by the RF power. Ions flow toward the boundaries where they are accelerated by the grid system and form the ion beam, thus generate thrust for the thruster.
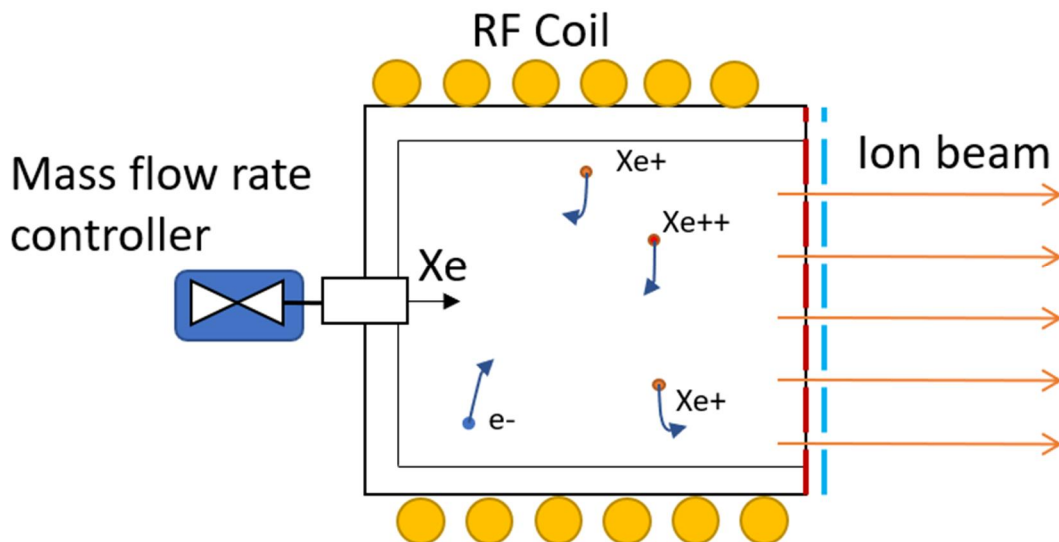
Figure 2.3 RF ion thruster operation (propellant: xenon)

An RF ion thruster system includes these sub-parts:

- RF power supply

- Grids power supply

- Gas feeding system

- Neutralizer

- RF ion thruster

2.2.2 RF inductively coupled plasma discharge in RF ion thruster

A plasma is a gas consisting of freely moving charged particles and neutral particles in random directions. On average, it is electrically neutral. The charged particles' movement is in response to the electric field of local moving particles as well as remote regions. At low frequencies, plasmas might act like conductors. However, at adequately high frequency, plasmas tend to exhibit more properties of a dielectric medium. By far, plasma is the most popular matter's state in the visible universe. Its occurrence usually exists in a vacuum. In space, observable plasmas states are the stars, galaxy, gaseous nebula... In our atmosphere, the occurrence of the natural observable plasma events is limited to some phenomena like a lightning bolt, the glow of the Aurora Borealis... Plasmas existing in our daily life could be named: the glow of the fluorescence lamp, the plasma screen pixel... The plasmas used in RF ion thruster is the weakly ionized type, which contains charged particles like ions and electrons and the neutral particles at low pressure.

In RF ion thruster, inductively coupled plasmas (ICP) discharge is utilized. The principle is to initiate an induced RF current into plasma by coupling the RF current in a coil. Inductive sources have advantages of a simple concept, no requirements of DC magnetic fields, using RF rather than microwave frequency. Two source configurations are usually used for ICP discharge: cylindrical and planar coils. In Figure 2.4a, the plasma is generated in a cylindrical dielectric chamber wrapped around by a cylindrical coil. Figure 2.4b shows the plasma being processed by a spiral planar coil, separated by a dielectric window.

(a)

(b)
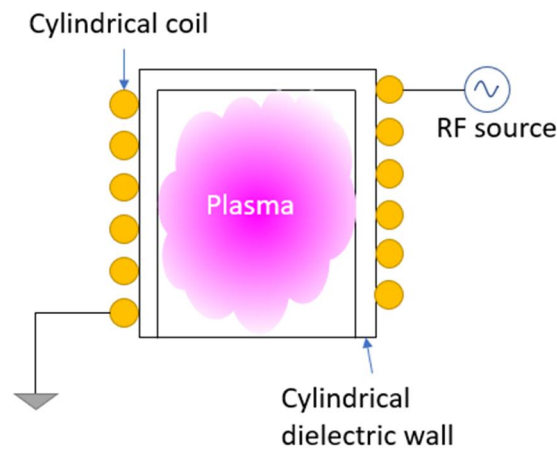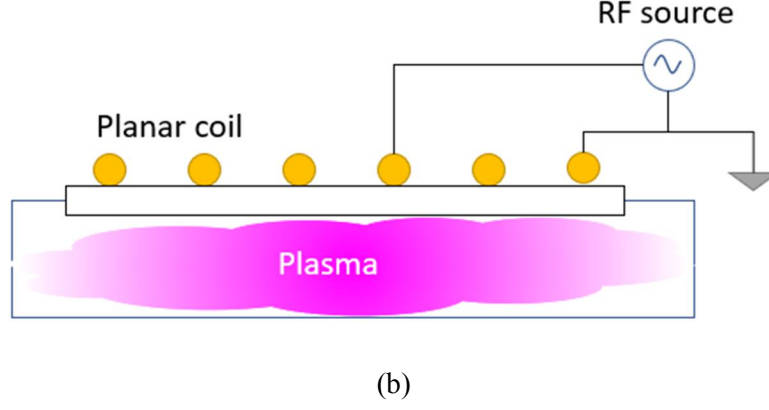
Figure 2.4 ICP source coil configurations (a) cylindrical; (b) planar

ICP discharge in the cylindrical coil configuration is usually modeled by a transformer model. Simple analysis for the proposed transformer model was introduced in 1992 by Piejak [19]: the coil and the plasma form a transformer where plasma is regarded as the secondary coil with one turn in an air-cored and the primary coil is the RF coil with resistance and inductance is R_{coil} and L_{coil}, respectively. This transformer model could be changed into an equivalent circuit as in Figure 2.5 with resistance and inductance are R_s and L_s.
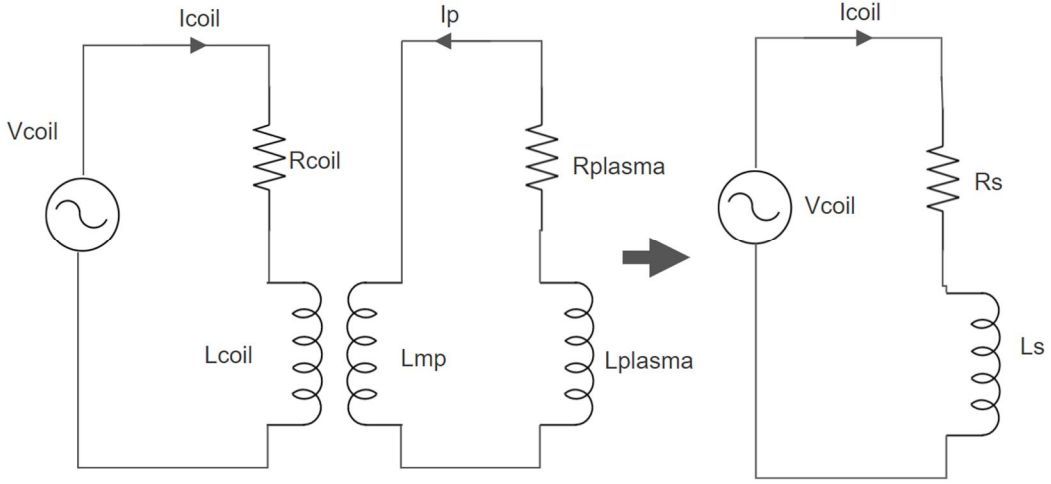
Figure 2.5 ICP discharge in transformer model and its equivalent circuit

By applying Kirchoff's laws to the above circuit, we can get:

$$V_{coil} = i\omega L_{coil} I_{coil} + R_{coil} I_{coil} + i\omega M I_P \qquad (2.12)$$

$$V_P = i\omega L_{mp} + i\omega M I_{coil} - I_P \left[R_P + i R_P \left(\frac{\omega}{v_m} \right) \right] \qquad (2.13)$$

$$V_{coil} = I_{coil} R_s + i\omega I_{coil} L_s \qquad (2.14)$$

Apply the electromagnetic model for ICP used in [20], the accurate description of equivalent resistance and inductance could be formulated as:

$$R_s = R_{coil} + R_P \frac{|I_P|^2}{I_{coil}^2} \qquad (2.15)$$

and

$$L_s = L_{coil} - \left(L_{mp} + \frac{R_P}{v_m}\right)\frac{|I_P|^2}{I_{coil}^2} \qquad (2.16)$$

By using this model and plasma parameters extracted from an analytical model (plasma density, RF coil current, absorbed power...), the plasma impedance transformation could be accurately approximated.

2.2.3 RF power supply system in an RF ion thruster

A block diagram of the RF power supply system in an RF ion thruster for small satellites is presented in Figure 2.6. The electrical power sources in small spacecraft systems are usually from solar cells or batteries and come in DC power. The microelectronics on spacecraft are capable of generating RF signal at the required frequency and to boost that signal to the required power, an RF power amplifier is needed. Switch-mode amplifiers like class D or class E RF amplifiers are commonly used. With the achieved RF power, a matching network is vital in keeping the maximum power transfer efficiency to the RF ion thruster (coil and plasma). Since the plasma is not a fixed load, tunable components are preferred in this circuit. L-matching network is a commonly used configuration. The topology selected for developing the RF power supply system is a class-E RF power amplifier and tunable L-matching network.
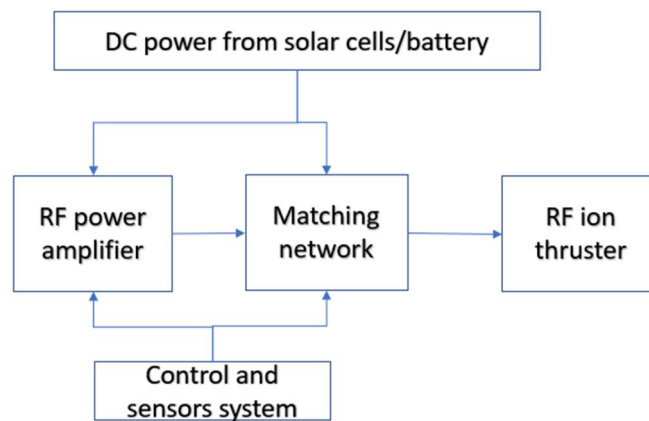
Figure 2.6 RF power supply in RF ion thruster system

Some popular configurations of RF system in RF ion thruster are:

- RIM – 4 Thruster: Half-bridge power amplifier developed in University of Giessen [10]

- BIT – 3 RF Ion Thruster: Dual channel RF power generator [21]

- RIT – 10 RF Ion Thruster: 2-stage electron-tube generator [6], half-bridge RF generator [22]

- 1 cm Miniature RIT (MRIT): RF power lab model + ML 50 RF amplifier [23]

- MiDGIT thruster: Research amplifier 75A250A power amplifier + MFJ-934 antenna tuner [24]

2.2.3.1 Class E RF power amplifier – Zero voltage switch method

Class E amplifier has the basic circuit as in Figure 2.7. It includes an input driver stage, which operates at frequency $f = \omega/(2\pi)$. This stage is used to control a power MOSFET which acts as a switch. The circuit also consists of an RF choke inductor L_f to reduce AC ripple on DC supply voltage, a shunt capacitor C_1 which comprises the transistor output capacitance and any external capacitance in parallel with it [25] and an RLC resonant network with R is an AC load.
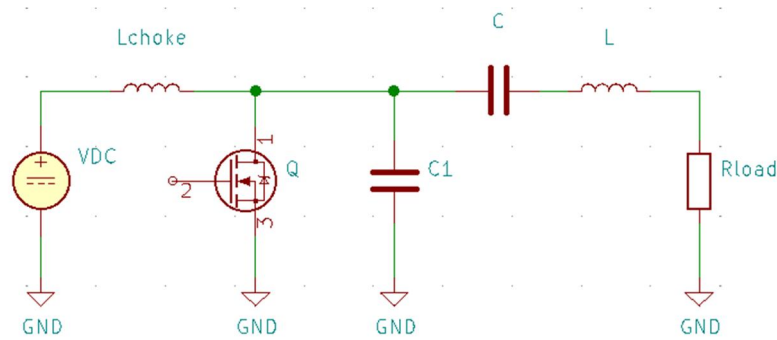
Figure 2.7 Class E RF Power Amplifier circuit

The load network is designated by 2 resonant frequencies. When the switching device is turned ON, the shunt capacitor is short-circuited, hence the resonant frequency will be:

$$f_{o1} = \frac{1}{2\pi\sqrt{LC}}$$

(2.17)

When the switch is OFF, capacitance of the resonant circuit will be:

$$C_{eq} = \frac{CC_1}{C + C_1}$$

(2.18)

Therefore, the resonant frequency in this case will be:

$$f_{o2} = \frac{1}{2\pi\sqrt{LC_{eq}}}$$

(2.19)

Circuit operation and ZVS operation:

In some circuits with semiconductors, there exists hard-switching operation in those components like pulse width modulation (PWM) power converters, digital gates.. [26]. Those circuits encounter switching losses. It happens when the voltage waveform drops rapidly from a high point to about zero when the switching components is turned ON. In the period just before turning ON, there is energy stored in the capacitor of the transistor C which has the value:

$$W = \frac{1}{2}CV^2 \qquad (2.20)$$

with V is the supply voltage to the transistor, usually the DC supply voltage. After the switching device is turned ON, the current goes to r_{DS} – ON-resistance of the transistor and the energy stored is conversed to heat. By taking switching frequency into account, the switching power loss could be calculated as:

$$P_{sw} = \frac{1}{2}fCV^2 \qquad (2.21)$$

However, the switching power loss could be prevented by putting the voltage across the transistor - v_{DS} to zero at the switching transition.

This is the principal idea of class E ZVS power amplifier: the transistor turned ON at zero voltage (ZVS). This type of operation is called *soft switching* generally.
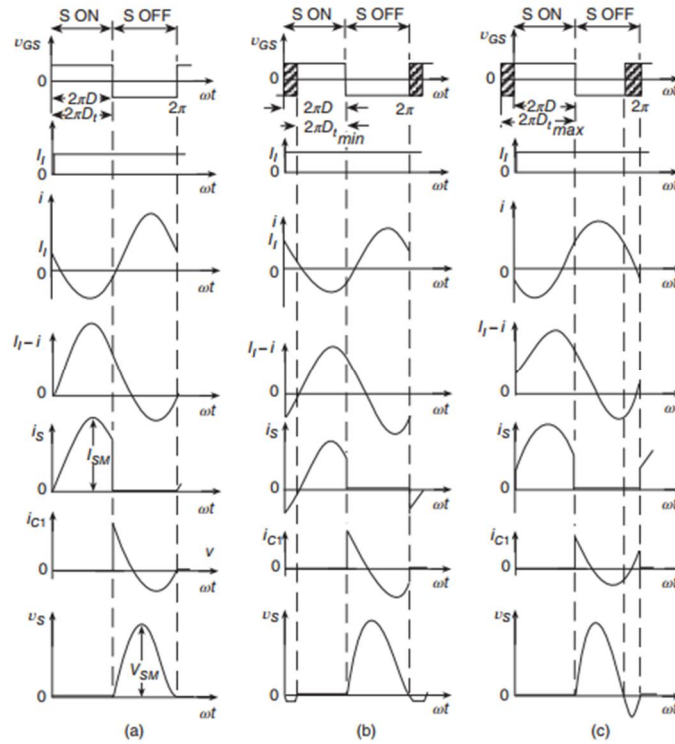
Figure 2.8 Waveforms in Class-E ZVS circuit. (a) Optimum operation. (b) Suboptimum operation with dvs (ωt)/d(ωt)<0 at ωt=2π. (c) For suboptimum operation with dvs (ωt)/d(ωt)>0 at ωt=2π. Image from [1]

In Figure 2.8, three cases of class-E ZVS circuit are shown and in all of them, the voltage across the transistor and the shunt capacitor is zero at the moment of turning ON. As a result, the energy loss will be zero in both the transistor and capacitor. The ZVS condition [1] therefore could be expressed as:

$$v_S(2\pi) = 0 \qquad (2.22)$$

To realize ZVS, the controlled frequency of the switch f should be greater than the resonant frequency $f_{o1} = 1/(2\pi\sqrt{LC})$ and lower than the frequency $f_{o2} = 1/(2\pi\sqrt{LC_{eq}})$ [26]. The quality factor Q_L will decide the shape of the current waveform i. It will be approximately sinusoidal at high Q_L and close to an exponential function at low Q_L [1]. ZVS optimum operation will also require the load resistance at the value close to the optimum resistance $R \cong R_{opt}$. When $R > R_{opt}$, the current flowing through the resonant tank network is smaller than the needed value, and as a consequence, the voltage drops at C_1 will decrease. The switch voltage is accordingly greater than zero at switching ON, increasing switching loss. In the opposite case where $R < R_{opt}$, current flow increases, voltage drop increases thus makes the switch voltage smaller than zero at the switch ON moment. In either case, the switching loss will increase to the value of $W = \frac{1}{2}C_1v^2$ at every RF period. However, the calculated optimum resistance is normally an odd or unconventional number.

In some applications, the load resistance could be adjusted over a certain range. The zero voltage at switching ON could be achieved in suboptimum operation for $R < R_{opt}$. The current flow in resonant circuit is increased. In this type of operation, the switching voltage at turning ON point is still zero but the derivative of switching voltage with respect to the ωt, $dv_s/d(\omega t)$ could be greater or smaller than zero. This operation waveform is depicted in the Figure 2.7 (b) and (c). The turn ON duty cycle of the switch in these operations is shorter than the system operating duty cycle thanks to the acceleration of the turn ON switching by the antiparallel diode integrated in power MOSFET. Advantage of this type of operation is utilization of ZVS at a more flexible load range. This allows the use of the non-ideal components. Practically, a load transformation technique will be used such as using transformer or LC matching network to change to load resistance to a conventional one (like 50Ω or 75Ω). Additionally, a series diode could be added to enhance the ZVS operation of the transistor. The disadvantage of the coupled diode circuit is increasing of turn ON voltage and conduction loss.

2.2.3.2 RF Impedance matching

In the design of RF circuitry, matching networks are usually obligatory for maximal power transfer efficiency between a source and its load. In DC circuits, maximum power transfer will happen when the load resistance equals to its source resistance. This can be easily proved in a simple circuit in Figure 2.8.
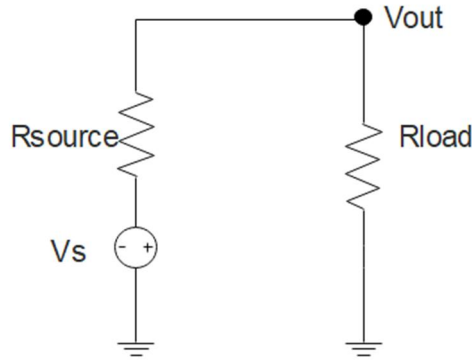
Figure 2.9 DC circuit

We have output voltage equals:

$$V_{out} = V_S \frac{R_L}{R_L + R_S}$$ (2.23)

Output power will be:

$$P_{out} = \frac{V_{out}^2}{R_L} = \frac{V_S^2 \left(\frac{R_L}{R_L + R_S}\right)^2}{R_L} = V_S^2 \frac{R_L}{(R_S + R_L)^2}$$ (2.24)

P_{out} is maximized when $R_L = R_S$. In an alternative current (AC) circuit, that same theory could be stated as the maximum power transfer happens when the load impedance Z_L equal to the complex conjugate of the source impedance. Complex conjugate is simply defined as a complex having the same real part but with an opposite imaginary part. The complex conjugate of $Z_S = R + jX$ will be $Z = R - jX$. This could be proved the same way as in the DC circuit. In the sum of Z_S and Z_L, the imaginary part will be canceled out, leaving only the real part, which follows the same as above. The matching network scheme is making the load looks like the load in the specified frequency. There are numerous possible networks for matching purposes, from simply two components network to something complicated 7-element network.

The L network is considered the simplest and most vastly used topology for matching networks. Some circuit configurations of the L-matching network are presented in Figure 2.9.

17
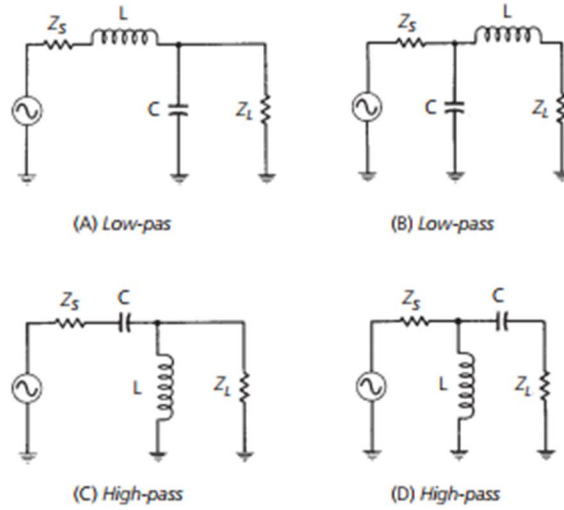
Figure 2.10 L-network configurations

In pure resistive load and source, the design of the matching network can be easily designed by the following equations from [27] with the circuit as in Figure 2.10.
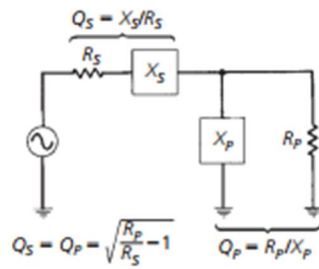
Figure 2.11 L-network component

$$Q_s = Q_p = \sqrt{\frac{R_p}{R_s} - 1} \qquad (2.25)$$

$$Q_s = \frac{X_s}{R_s} \qquad (2.26)$$

$$Q_p = \frac{R_p}{X_p} \qquad (2.27)$$

where the subscript s denotes the series leg and p denotes the shunt leg. When dealing with complex load, two basic techniques could be used are Absorption and Resonance. The absorption method is to absorb any stray reactance into the matching network itself. Resonance is to resonate the stray reactance with opposite reactance at the specified frequency. In the matching network for RF ion thruster, the resonance approach is preferred. The calculation of such a matching network circuit will be described in Chapter 4.

3 RF ion thruster plasma investigation

3.1 Plasma prediction based on the analytical model

3.1.1 Analytical model of discharge chamber descriptions

A 0-D analytical model for discharge chamber has been developed at Applied Aerospace Research Laboratory (AARL) in the University of Ulsan [28]. The goal of this model is to deepen the understandings of the processes occurring in the discharge chamber during RF ion thruster operation. A flow chart of the model is presented in Figure 3.1:
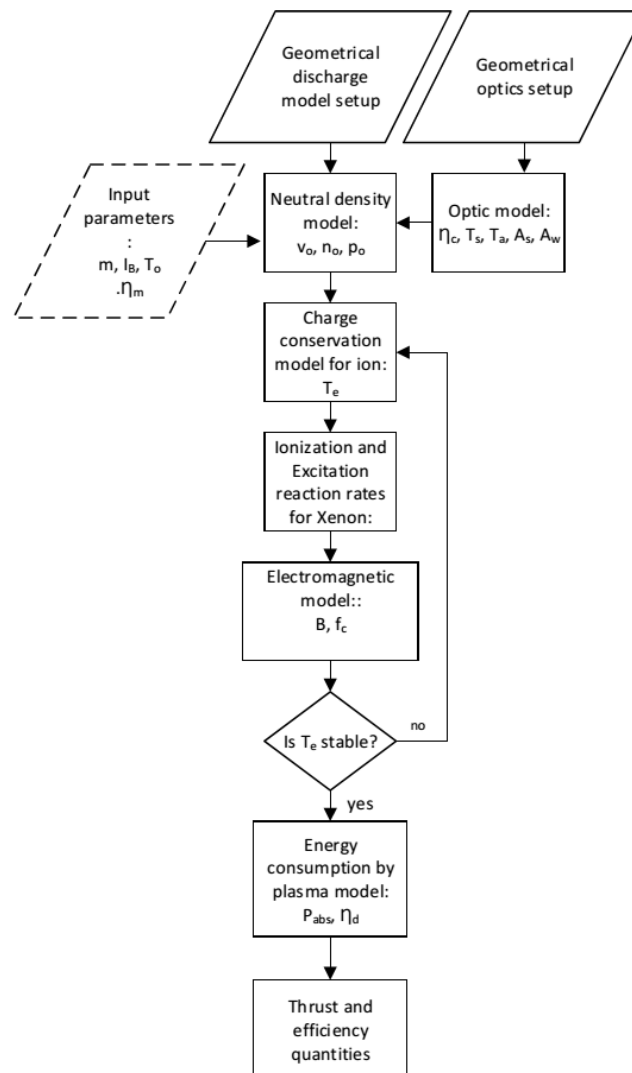
Figure 3.1 Analytical model for RFIT discharge flow chart

The analytical model takes geometrical data of discharge chamber and optics system and initial parameters such as excitation and ionization energy of the propellant, gas temperature as inputs. The optics system properties including grids transparency, Clausing factor are calculated next. Then the neutral density, charge conservation, electromagnetic model, and energy consumption model are

19

utilized to compute the plasma's important characteristics such as pressure, plasma density, plasma potential... and plasma performance parameters as well.

3.1.2 iU-50 descriptions

The iU-50 was developed at AARL in the University of Ulsan. Following the previous version, the iU-50 (2021) RF ion thruster kept the truncated conical shape with slight modifications in discharge chamber geometrical parameters. The ion optics system is a 2-grid configuration that consists of a screen grid and an acceleration grid. The discharge chamber of the thruster is made from alumina ceramic which has been proved to have good mechanical properties and flexible ionizer design capabilities. Grids system's material is Molybdenum which is a weak paramagnetic material [29] and suitable for CNC machining. Detailed parameters of the iU-50 will be presented in Table 3.1.

Table 3.1 iU-50 parameters

Discharge chamber	
Parameters	**Value**
Beam diameter	50
Diameter at the grids	55
Length of the chamber	40
Back diameter(mm)	16
Material	Alumina ceramic
Ion optics system	
Parameters	**Value**
Number of apertures	547
Screen grid hole diameter (mm)	1.6
Screen grid thickness (mm)	0.8
Screen grid voltage (V)	1000
Acceleration grid hole diameter (mm)	1.1

Acceleration grid thickness (mm)	0.55
Acceleration grid voltage (V)	-150
Material	Molybdenum

The iU-50 RF ion thruster peripheral components include a gas inlet, RF coil, and casing. The gas inlet is a 1/8" stainless steel pipe connected with a thermal isolator through a Swagelok fitting. The RF coil wound around the discharge chamber is made from the enameled copper AWG 12 and has 10 turns. A case made of aluminum was designed and manufactured for the thruster. A 3-D model of the thruster is shown in Figure 3.2.
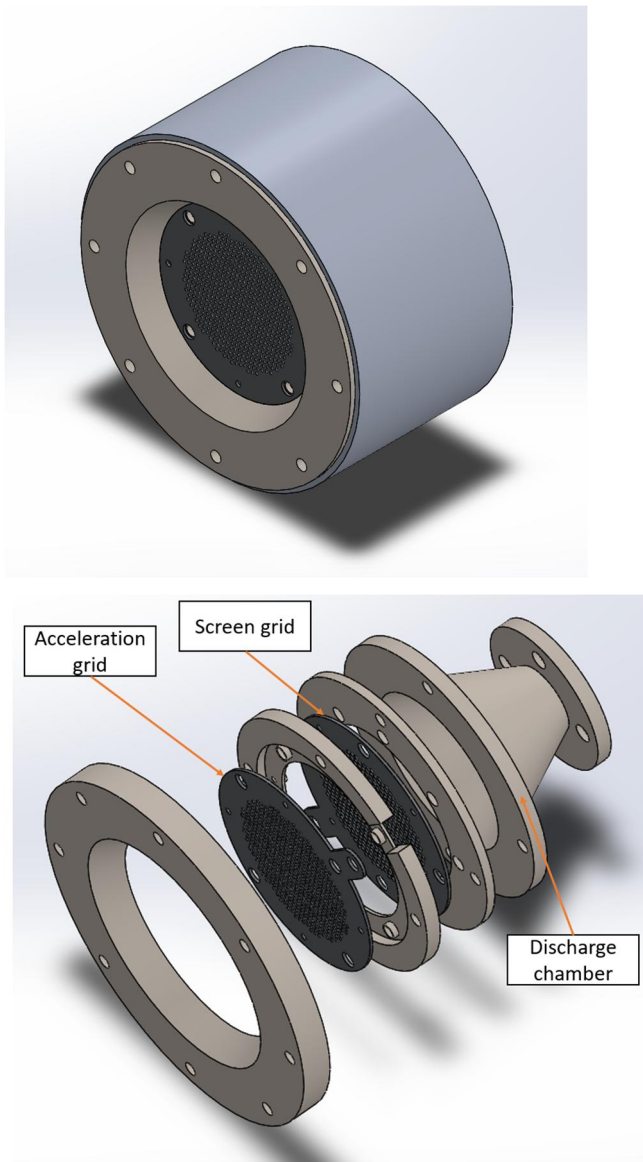
Figure 3.2 iU-50 CAD model and assembly

Evaluation parameters of the thruster design using the above analytical model are presented in Table 3.2.

Table 3.2 Evaluation parameters of iU-50

Parameter	Value
Power (W)	50
Mass utilization efficiency	84.4%
Pressure (Torr)	9.5E-05
Mass flow rate (sccm)	0.7902
Electron temperature (eV)	9.752
Plasma density ($1/cm^3$)	3.47794E+11
Ion beam current	0.05
Discharge loss (W/A)	1001.38

3.1.3 Plasma impedance analysis based on Analytical model

Plasma parameters in the RF ion thruster discharge chamber were computed using the analytical model. These parameters were used in deriving the transformer model parameter of the ICP discharge. First, the coil resistance and inductance were calculated normally by considering the coil's length, shape, diameter, and material. The diagram of such coil we are evaluating could be seen in Figure 3.3:
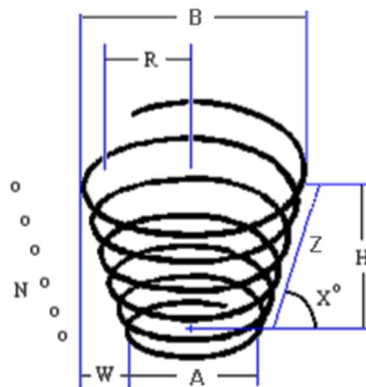
Figure 3.3 Truncated conical coil diagram.

The inductance is calculated based on the empirical Harold Wheeler formulas. Vertical and horizontal components of inductance are denoted by L_1 and L_2 respectively and calculated by:

$$L_1 = \frac{R^2 N^2}{9R + 10H} \tag{3.1}$$

$$L_2 = \frac{R^2 N^2}{8R + 11W} \tag{3.2}$$

where:

N – number of turns

A – diameter at the base of the cone

B – diameter at the top of the cone

H – the height of the coil

$W = (B - A)/2$ – effective radius of the coil

$R = A/2 + W/2$ – average radius of the coil

X – the angle of the cone that $\sin(X) = H/Z$; $\cos(X) = W/Z$

The aggregate inductance of the coil will be:

$$L = \sqrt{(L_1 sinX)^2 + (L_2 cosX)^2} \tag{3.3}$$

The resistance of the coil would be calculated by the equation of a wire resistance as:

$$R = \frac{\rho L}{A} \tag{3.4}$$

where:

ρ – resistivity of the wire

L – length of the wire

A – cross-sectional area

After calculating the coil's inductance and resistance, we can move on to the ICP transformer model as introduced in Chapter 2. The equivalent series resistance and inductance in the transformer model are as follows [20]:

$$R_S = R_{coil} + R_{ind} \tag{3.5}$$

$$L_s = L_{coil} - L_{mp}\left(\frac{R_{ind}}{R_p}\right) - \frac{R_{ind}}{v_m} \tag{3.6}$$

where R_{ind} and L_{ind} are the resistance and inductance of the system derived by the electromagnetic model. At high electron density regime ($> 10^{16}(1/m^3)$), the inductance term can be approximated by:

$$L_s \approx L_{coil}\left(1 - \frac{r_0^2}{r_c^2}\right) \qquad\qquad (3.7)$$

where r_0 and r_c are the inner and outer diameter of a cylindrical discharge chamber. In the case of the truncated conical shape discharge chamber, the radius values were averaged can the value of the equivalent inductor could be calculated. The electromagnetic resistance could be figured from the absorbed power parameter by:

$$R_{ind} = \frac{2P_{abs}}{I_{coil}^2} \qquad\qquad (3.8)$$

Hence, from analytical model results, the system of plasma and coil resistance and inductance could be predicted. Then the impedance at the operating frequency can be used in the design of the RF power supply system.

3.2 2-D axisymmetric plasma simulation

3.2.1 VizGlow plasma simulation suite

VizGlow is an industrial simulation tool for modeling non-equilibrium plasma discharge [30]. VizGlow models of plasma use well-established continuum/fluid formulation of the plasma governing equations. It is capable of modeling and solving plasma phenomena in 3-D, 2-D, and even 1-D problems. Its features according to the homepage [31] are as the followings:

- D, 2-D (planar/axisymmetric) and 3-D problems

- Self-consistent (sheath + plasma) and quasi-neutral formulation

- Multi-species, multi-temperature formulation

- Finite-rate gas chemistry (complex gas mixtures) and surface chemistry (etching, deposition, etc.)

- Coupling to electromagnetics and fluid-flow

- Coupling to kinetic particle models for hybrid plasma simulation

- Photoionization model

- General circuit model

- Valid over the range of pressures ~mTorr to 10+atm.

- Unstructured mixed mesh framework

- Parallel computing

With high capabilities of modeling and computing, VizGlow is suitable for modeling many types of plasmas, including capacitively coupled plasma (CCP), ICP, microwave plasmas (MWP), DC

plasmas... Figure 3.4 shows the physics modules that can be coupled with VizGlow software to model and solve different types of problems.

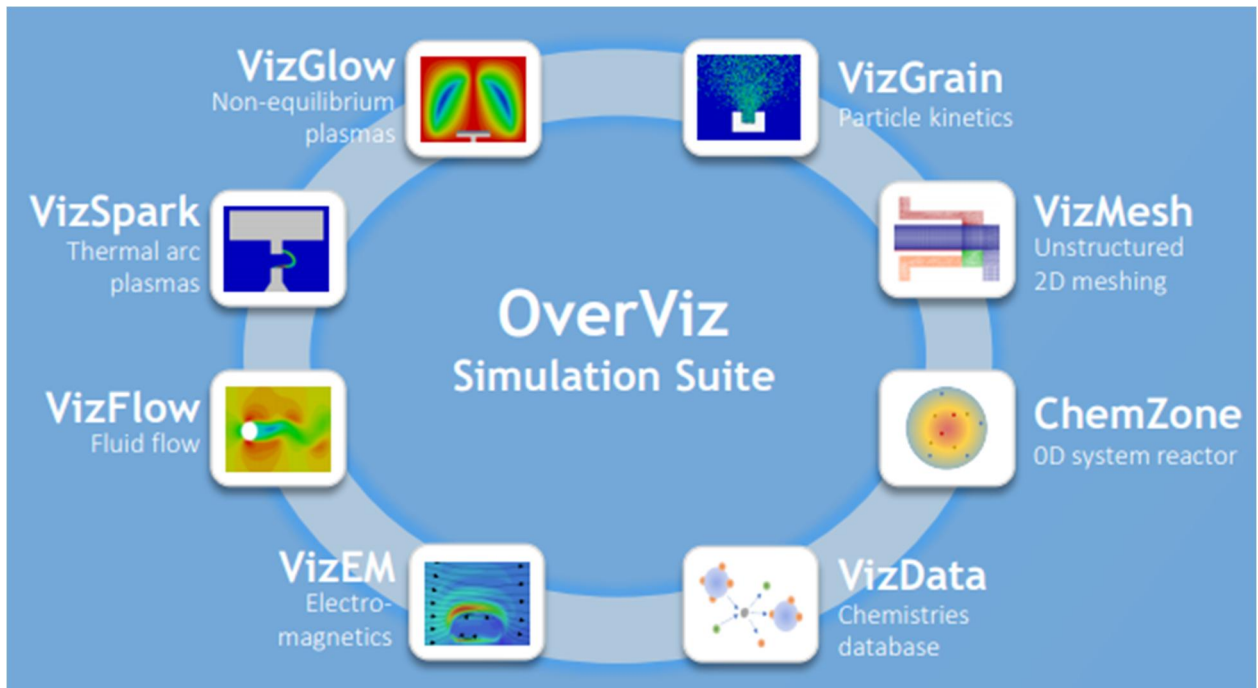*Figure 3.4 OverViz simulation suite physics modules*

3.2.2 RF ion thruster simulations

Simulations of the RF ion thruster developed at AARL in the University of Ulsan – the iU-50 have been carried out. The dimensions for the model are from the description parameters in section 3.1. The simulations utilized the 2-D axisymmetric model, with the axis is the x-axis. Figure 3.5 describes the model of the simulation.
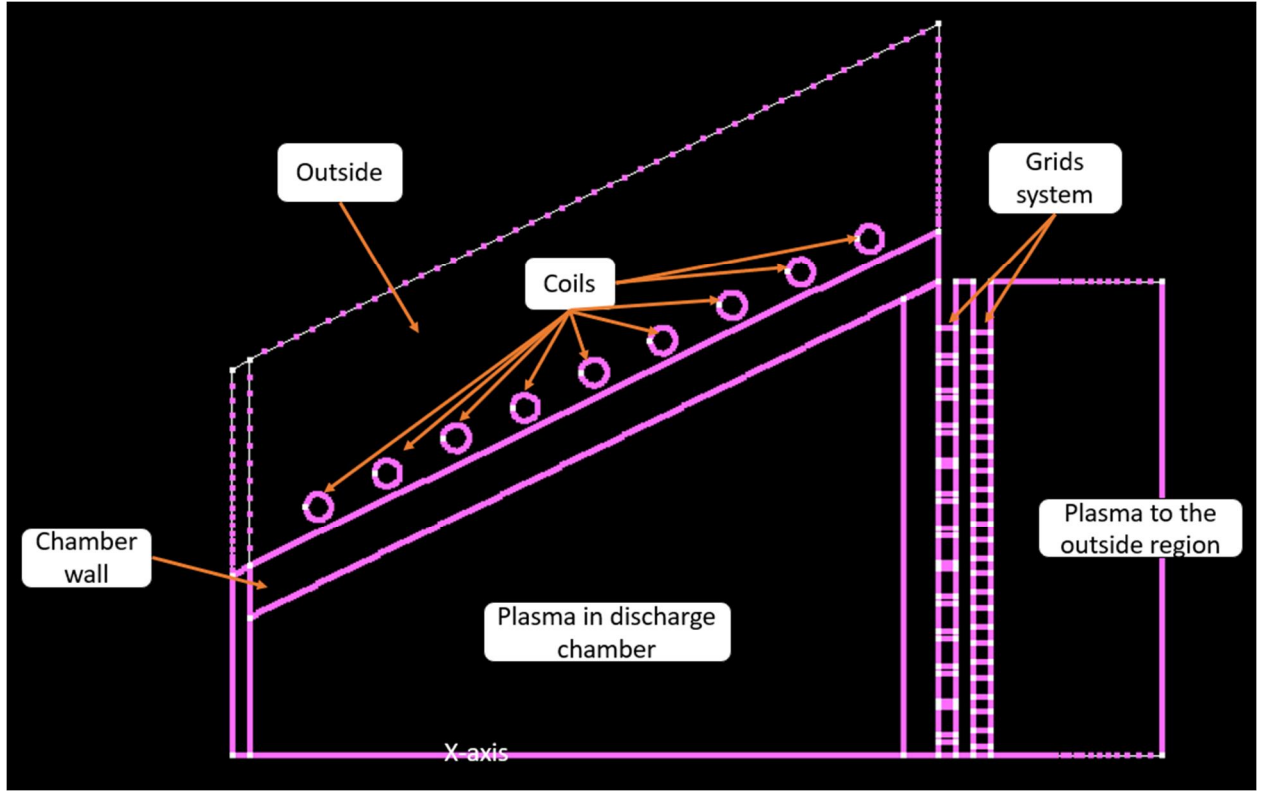
Figure 3.5 Simulation geometry model

The simulation model will solve plasmas equations in the regions inside the discharge chamber and at the exhaust. The chamber wall is modeled as an insulator. The grids system is coupled with external circuits to represent the real grids system with positive high voltage to screen grid and negative high voltage to the acceleration grids. The coil region represents the RF coil wrapped around the discharge chamber and was coupled with RF power in the simulation. The outside region at the side of the engine is used to observe the electrostatic potential and electromagnetic wave around the outside of the discharge chamber.

A mesh was created for the computational domain. It is finer at the concerned regions like in the discharge chamber sub-domain and rougher in others. The smallest edge mesh element has a value of 0.107 (mm) – near the grids area and the largest has a value of 1.01 (mm) at the outside. The type of cell element is the triangle element since the quad-element would not be utilized in this geometry.

The governing equations solved in this simulation are:

The species continuity equation is given as:

$$\frac{\partial n_k}{\partial t} + \nabla \cdot f_k = \dot{G}_k + \frac{1}{\tau_{flow}}\left(n_k^{in} - n_k\right) \tag{3.9}$$

The species continuity equations in this simulation are subjected to the Ideal gas law with the specified known pressure in the gas. The equations are solved only in the plasma region. Boundary conditions for this equation are that solid surface flux is defined at the chamber wall and grids. The continuous

condition is applied at the boundary between inside and outside the discharge chamber. The axis condition is applied at the x-axis.

Ion momentum equation:

$$\frac{\partial}{\partial t}(n_i \vec{u_i}) + \vec{\nabla} \cdot (n_i \vec{u_i}\vec{u_i}) = \frac{eZ_i}{m_i} n_i \vec{E} - \frac{1}{m_i} \vec{\nabla} p_i - n_i \bar{v}(\vec{u_i} - \vec{u})$$ (3.10)

Electrostatic potential: the electrostatic potential in the plasma discharge could be established by solving Gauss's law in Maxwell's equations of electromagnetic. In the case of non-zero space charge, Gauss's law can be represented by Poisson's equation as:

$$\nabla \cdot (\epsilon_r \nabla \phi) = -\frac{\rho_c}{\epsilon_0}$$ (3.11)

The electrostatic potential is solved for all the computational domains. The boundary conditions applied for this simulation are as follows: Fixed potential at the outside boundary, the external circuit at the grids, and continuous at the borders of each sub-domain.

Electron energy conservation equation. Electron temperature could be determined in two different ways: either solving the electron energy conservation equation or using the Local Field Approximation (LFA). Electron temperature is solved in the plasma region only. Boundary conditions are applied as follows: Solid surface flux at the walls and fixed temperature at the predetermined boundaries.

Electromagnetic wave. The electromagnetic wave equations are solved in the frequency domain. Maxwell equations are used to determine the electromagnetic field in any medium (plasma, gas, solid, and liquid). The electromagnetic equations in the frequency domain are solved for all computational domains. The coils sub-domain is applied RF current with power control. The boundaries condition mainly used is a perfect electric conductor for a boundary.

A standard operation at 50W, 3 MHz RF power was simulated using those above equations and boundary conditions. The simulations were also carried out with different powers and frequencies to establish the effect of these parameters on the plasma characteristics and impedance.

4 Design of RF Power Supply system

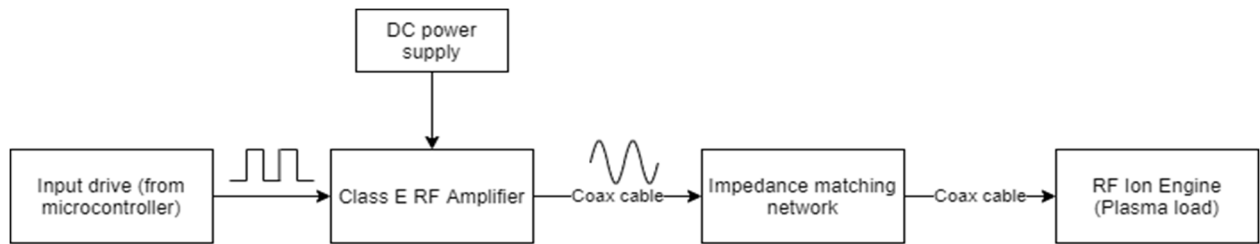## 4.1 RF Power Supply system description

Figure 4.1: RF power supply system diagram

The diagram of the RF power supply system is presented in Figure 4.1. The system concept is as follows: The microcontroller generates a small square signal at the precise predetermined frequency. This signal will be of use to drive the RF Amplifier. The RF Amplifier utilizes a DC power source and boosts the RF signal to the required Power level. The RF power signal will go through an Impedance matching network for maximum power transfer efficiency to the coil of the Engine.

System components:

- Input drive: We use a microcontroller (STM32F405RG) to generate the drive signal. This microcontroller can be integrated into the main controller to control the frequency level of the RF generator.

- Class E RF Power Amplifier: We choose class E RFPA topology for its simplicity and high-power conversion efficiency. This topology utilizes the transistor operating as a switch.

- DC power supply: We use a laboratory DC power supply for the prototype circuit but on the satellite, where the RF Ion Thruster is put into service, the RF Generator system will be powered by a DC source from solar cells or battery.

- Impedance matching network: RF Power Amplifiers are generally designed to run effectively for a fixed load. Therefore, an impedance matching network from the designated load to the dynamic plasma load is essential for an efficient power transfer. We used L-matching topology for this component.

4.2 Design of class E power amplifier:

4.2.1 Design equations

The design of the class E RF amplifier is following the analysis in [26]. There are some assumptions before analyzing:

1 – The transistor and enhanced components (diodes) form an ideal switch (ON-resistance is 0; OFF-resistance is infinity).

2 – The choke inductor is at a high value so that the AC component in the DC supply voltage can be negligible in comparison with the DC component.

3 – The quality factor of the resonant tank network is at a high value so that the current flowing through is in a sinusoidal shape

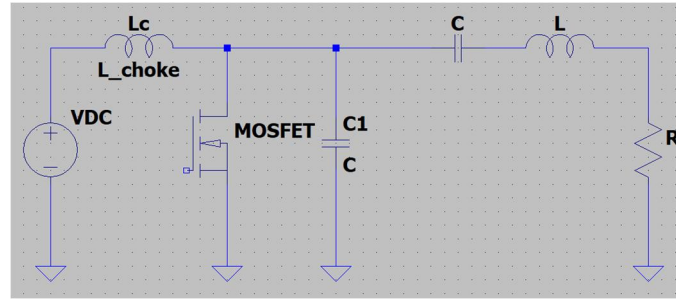4 – Operating duty cycle is 50%

Circuit analysis:

Figure 4.2 Circuit for analysis

The current and voltage at the resistive load, by assumption, are sinusoidal and can be represented as:

$$i = I_M \sin(\omega t + \phi) \qquad (4.1)$$

and

$$v = V_M \sin(\omega t + \phi) \qquad (4.2)$$

with $V_M = I_M \times R$ where I_M, V_M is the amplitude of the current and voltage waveform accordingly. ϕ is the initial phase.

By Kirchhoff's law, $i_S + i_{C1} = I_{DC} - i = I_{DC} - I_M \sin(\omega t + \phi)$.

In the period $0 < t < \pi/\omega$, the switch is ON and the current does not flow through the shunt capacitor, $i_{C1} = 0$. In the remaining time of a cycle, the switch is OFF and the current through MOSFET is zero, $i_S = 0$.

The voltage across the MOSFET and C_1 is:

$$v_{C1} = v_S = \frac{1}{\omega C_1} \int_0^{\omega t} (I_{DC} - I_M \sin(\omega t + \phi)) d(\omega t)$$

$$= \begin{cases} 0 & at \ 0 < \omega t \leq \pi \\ \frac{1}{\omega C_1}\{I_{DC}(\omega t - \pi) + I_M[\cos(\omega t + \phi) + \cos \phi]\} & at \ \pi < \omega t \leq 2\pi \end{cases} \qquad (4.3)$$

For ZVS conditions v_S at 2π is zero, the above equation becomes a connection between I_{DC}, I_M and ϕ:

$$I_M = -I_{DC}\frac{\pi}{2\cos\phi} \qquad (4.4)$$

Substitute this equation to the switch-across voltage equation we get:

$$v_S = \begin{cases} 0 & at\ 0 < \omega t \leq \pi \\ \dfrac{I_{DC}}{\omega C_1}\left\{\omega t - \dfrac{\pi}{2cos\phi}[cos(\omega t + \phi)] - \dfrac{3\pi}{2}\right\} & at\ \pi < \omega t \leq 2\pi \end{cases} \tag{4.5}$$

For the optimum operation, the derivative of switching voltage equal to zero at the turn ON point, that $dv_S/d(t) = 0$ at $t = 2\pi/\omega$. Applied in switch voltage, we get the phase angle of the waveform:

$$tan\phi = -\frac{2}{\pi}\ or\ \phi = 2.575\ (rad) \tag{4.6}$$

The voltage across the ideal choke that we assumed has a DC value of zero. Therefore, the DC supply voltage could be found:

$$V_{DC} = \frac{1}{2\pi}\int_{\pi}^{2\pi} v_S d(\omega t) \tag{4.7}$$

Using the equation of switch voltage and phase value:

$$V_{DC} = \frac{I_{DC}}{\pi\omega C_1} \tag{4.8}$$

and the DC supply resistance could be found as:

$$R_{DC} = \frac{V_{DC}}{I_{DC}} = \frac{1}{\pi\omega C_1} \tag{4.9}$$
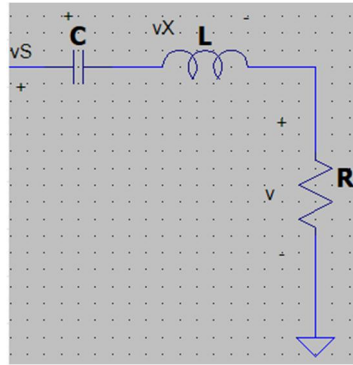
Figure 4.3 Voltage at resonant tank network

Coming back to the resistive load voltage v, at the resonant circuit, we have that $v = v_S - v_X$, with v_X is the voltage across L-C components as in Figure 4.3. The fundamental element of v_X is zero as the reactance of the tank network at the normal operating frequency is zero. At the resonant inductor, the voltage across is:

$$v_L = V_{LM}\ cos(\omega t + \phi) = \omega L I_M\ cos(\omega t + \phi) \tag{4.10}$$

Therefore,

$$v_S = v + v_L = I_M R\ sin(\omega t + \phi) + \omega L I_M(\omega t + \phi) \tag{4.11}$$

30

Using switch voltage equation and Fourier series formula, we can derive maximum voltage across the load resistor:

$$V_{RM} = \frac{1}{\pi} \int_{\pi}^{2\pi} v_S \sin(\omega t + \phi) d(\omega t) = \frac{4}{\sqrt{\pi^2 + 4}} V_{DC} \tag{4.12}$$

The resonant load network can be then calculated as:

$$R = \frac{V_M}{I_M} = \frac{8}{\pi(\pi^2 + 4)\omega C_1} \tag{4.13}$$

and

$$\omega C_1 = \frac{P_O}{\pi V_{DC}^2} \tag{4.14}$$

The reactance of the inductor depends on load resistance and chosen loaded quality factor Q:

$$\omega L = QR \tag{4.15}$$

And the reactance of resonant capacitor is:

$$\frac{1}{\omega C} = R\left(Q - \frac{\pi(\pi^2 - 4)}{16}\right) \tag{4.16}$$

Rewrite the values of the resonant network components (C_1, R, L, C) are presented in these equations at the optimum operation and duty cycle at 50%:

$$R = \frac{8}{\pi^2 + 4} \frac{V_I^2}{P_o} \tag{4.17}$$

$$C_1 = \frac{8}{\pi(\pi^2 + 4)\omega R} \tag{4.18}$$

$$L = \frac{Q_L R}{\omega} \tag{4.19}$$

$$C = \frac{1}{\omega R\left(Q_L - \frac{\pi(\pi^2 - 4)}{16}\right)} \tag{4.20}$$

Input's specifications of the RF power amplifier at the University of Ulsan are specified in Table 4.1:

Table 4.1 RF power amplifier specifications

Target specifications	Values
Power	$50(W)$
DC supply voltage	$100(V)$

Output frequency $3\ (MHz)$

Detailed designed calculations could be found in the Appendix. The theoretically calculated components for the class E power amplifiers are as in Table 4.2:

Table 4.2 Calculated parameters of the RF power amplifier.

Parameters	Value
Optimum load resistance (R_{opt})	115.36 Ω
Choke inductance (L_f)	$\geq 270\ \mu H$
Resonant capacitor (C)	78.64 pF
Resonant inductor (L)	42.84 μH
External shunt capacitor (C_1)	84.43 pF
Efficiency (η)	96.97%

4.2.2 Circuit simulation

From 1965, computer-aided circuit simulations have been developed and applied to the design process but at a high cost and time-consuming [32]. Today, with the computational capabilities of computers, circuits with thousands of transistors, lumped-component, ICs... could be analyzed in simulation with ease. It has become a routinely used design tool, a design step in circuit design. In this part, we will go through the development and analysis of the simulation of the class-E power amplifier.

An electrical simulation of the class-E ZVS amplifier was conducted in LTSpice simulator software. LTspice is a high-performance SPICE (Simulation Program with Integrated Circuit Emphasis) simulation software. It offers the capabilities of modeling transistors, ICs, switching devices, lumped component... behaviors, observing and capturing the waveforms of voltage, current, and powers as well as providing a large library of components for use with ease. The computational ability of LTspice is enhanced, allowing it to simulate rapidly. This is a huge boost for adjusting and optimizing circuit components.

The circuit simulation model circuit for the class E power amplifier is shown in Figure 4.4. It includes the DC power supply with an assumed series resistance of 0.1Ω, the resonant network with L-transformation to 50Ω load comprised of the conventional inductors and capacitors value for easy fabrication of the prototype, and the signal generator utilized a square wave source. The MOSFET model used in this simulation is the IRF840 with characteristics similar to the chosen in theoretical

analysis. Its SPICE model's main properties are taken from the datasheet [33], shown in Figure 4.5. Fully description of the model will be attached in Appendix.
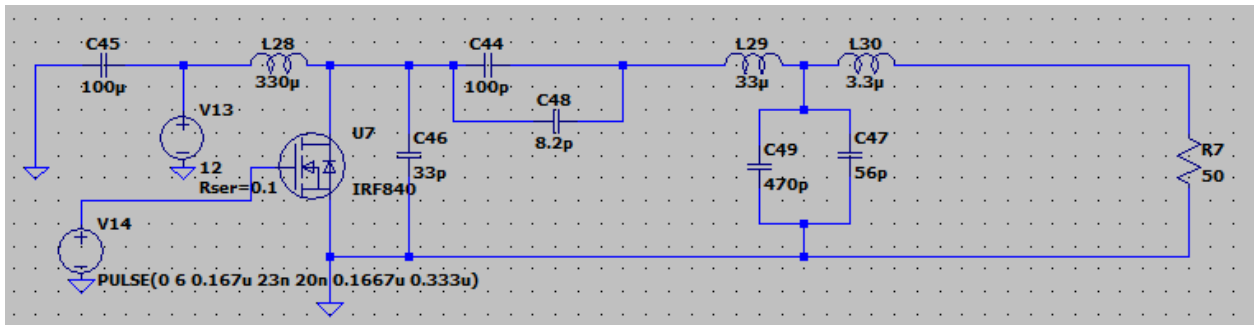

Figure 4.4 Circuit simulation diagram

| PRODUCT SUMMARY		
V_{DS} (V)	500	
$R_{DS(on)}$ (Ω)	V_{GS} = 10 V	0.85
Q_g max. (nC)	63	
Q_{gs} (nC)	9.3	
Q_{gd} (nC)	32	
Configuration	Single	

Figure 4.5 IRF840 electrical properties

The simulation was run in the time domain with a stop time of 200 (μs), which is about 600 RF cycles. With the DC power supply series resistance taken into account, the DC supply voltage took around 60 (μs) to reach the predetermined voltage of 100 (V). Therefore, the output voltage took that much time to be stabilized. The DC supply voltage was also free of AC ripples thanks to the high value of the choke inductor. Its waveform is presented in Figure 4.6 (a), the output voltage and power waveform were captured at the load. The voltage waveform is in sinusoidal shape with a small asymmetricity. The power waveform was integrated over time and show a desirable average power at 50W. Their waveforms are shown in Figure 4.6 (b) and (c) below:
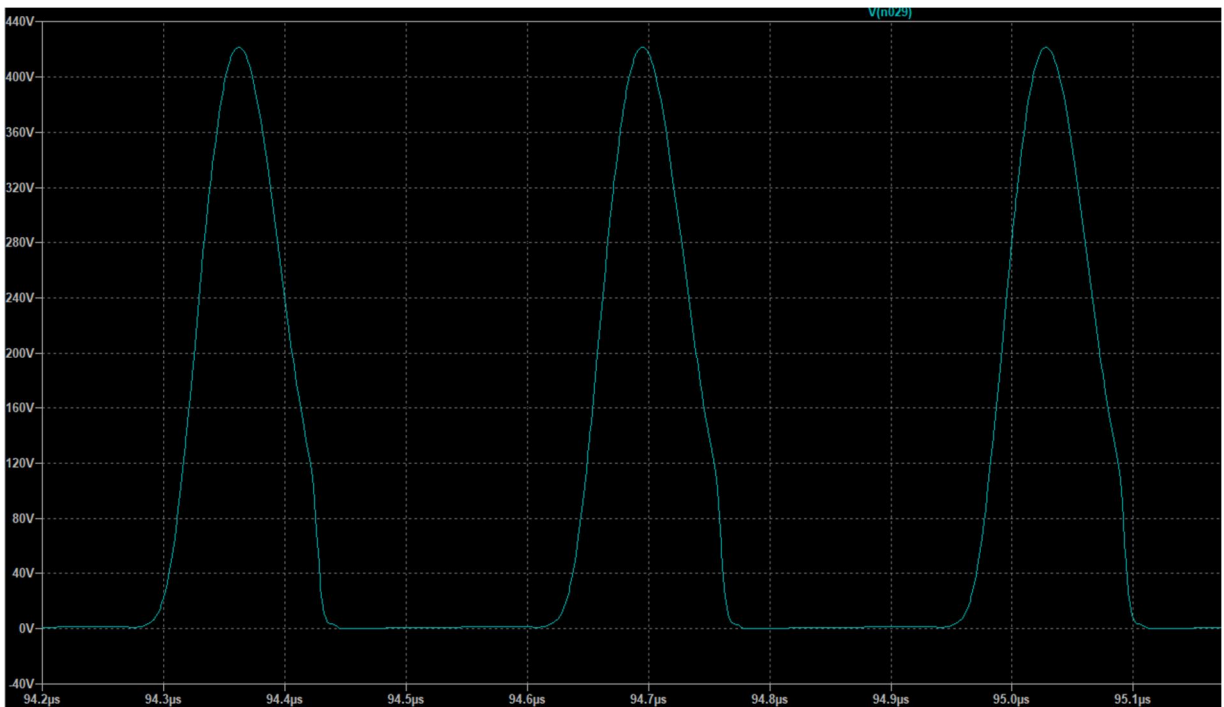
(a)

(b)

34
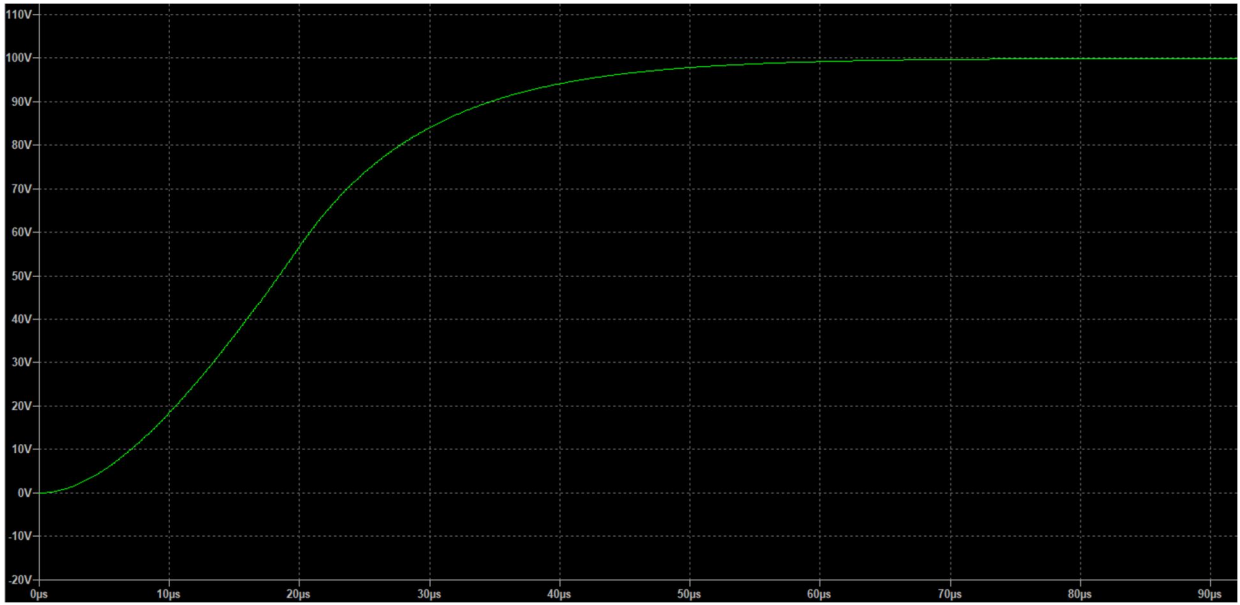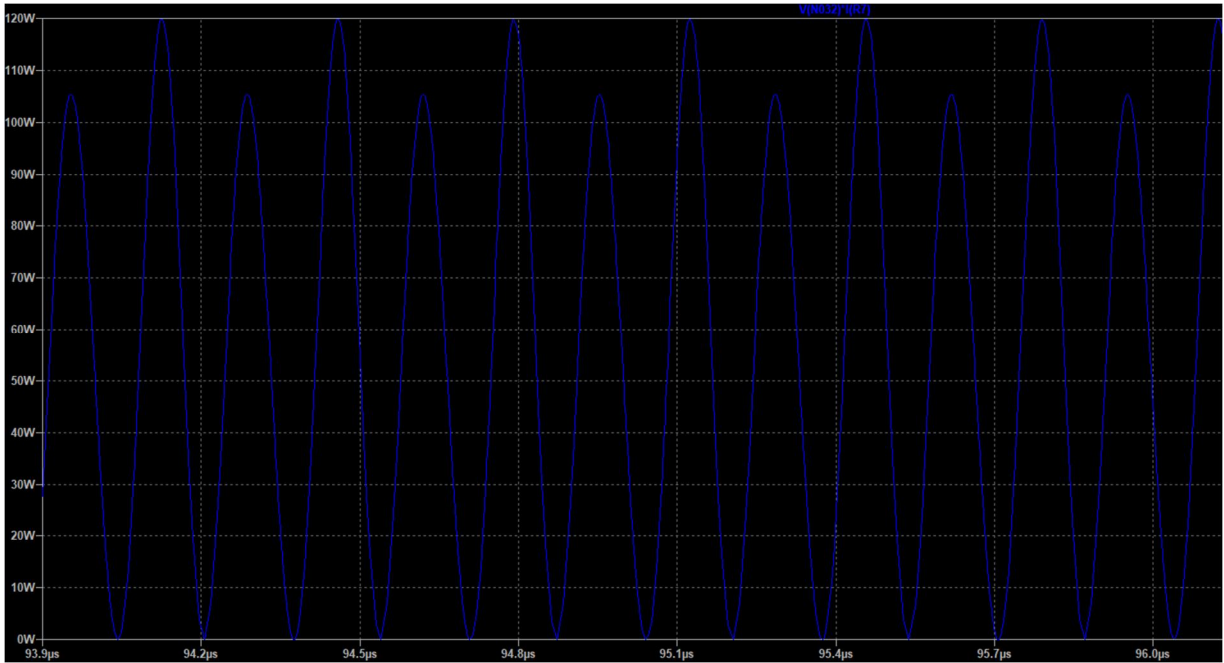
(c)

(d)

Figure 4.6 Waveform of (a)DC power supply; (b) output voltage; (c) output power; (d) drain junction voltage.

The drain junction voltage waveform shows that the analysis in the design equation is acceptable enough for choosing a power MOSFET with a high drain-source voltage V_{DS}. A few adjustments in the resonant tank network were done in order to use market-available components for the practical building of the circuit prototype as well as optimize the power output of the circuit.

35

4.2.3 Prototype circuit

With the help of the theoretical analysis and computer-aided simulation, a prototype circuit was planned and built. In this sub-section, the description of the prototype circuit will be presented. A diagram showing the RF generator system is presented in Figure 4.7:
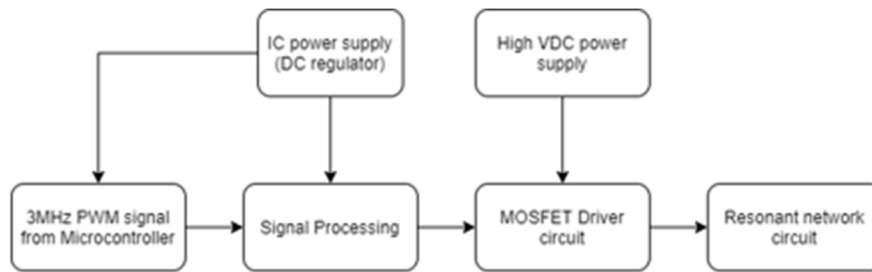

Figure 4.7 RF power amplifier prototype circuit diagram

The system is divided into several modules: DC regulators, Signal processing, a MOSFET driver circuit, and a resonant circuit. A 3MHz square wave signal is generated from Microcontroller. Then it goes through a signal processing circuit which includes an optocoupler and a Hex-Schmitt trigger used for isolating the high voltage and reduce the ringing of the signal. The output of the signal processing circuit is then going to the MOSFET Driver circuit and resonant network to produce a sinusoidal waveform that has the parameters as in specifications.

The DC regulator sub-circuit schematic is shown in Figure 4.8. The IC LM317 is utilized to provide a stable small DC power supply. The LM 317 is an adjustable 3-terminal regulator with the capability of supplying more than 1.5A [34]. It was selected due to the flexibility of the adjustable regulator and simple circuit configuration. Three levels of DC voltage were needed in the system: 5V, 12V, and 15V. The 5V level powers for the working of the integrated circuit (IC) chips. The 12V level supplies for heatsink fans that provide active cooling of the system and the 15V level is used for drive voltage of the MOSFET. In the schematic, there are variable resistors for modifying the voltages and diodes for reverse protection. Also, some electrolytic and ceramic capacitors were employed to improve stability and transient response.
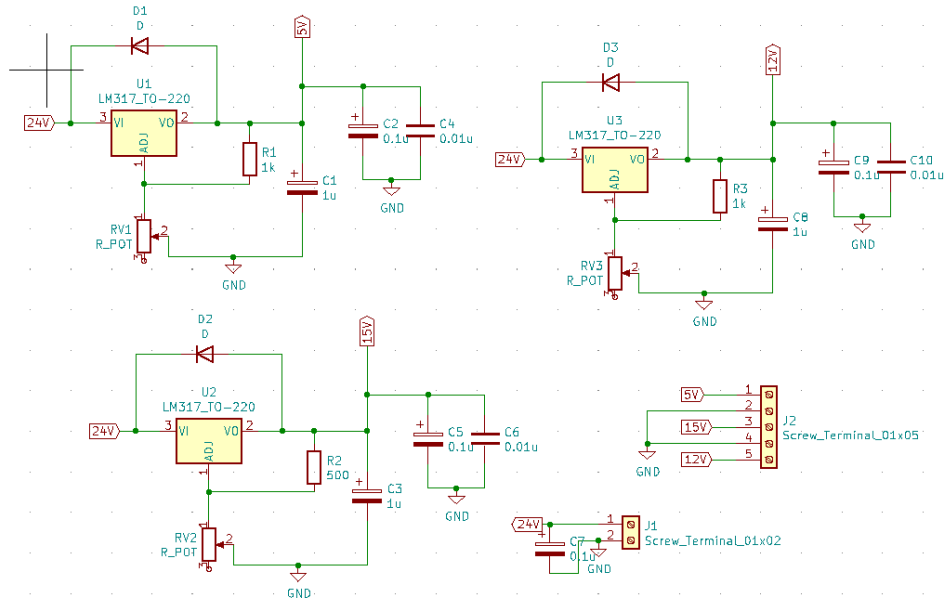
Figure 4.8 DC Regulator sub-circuit schematic

In the signal processing sub-circuit shown in Figure 4.9, a square wave signal at a specified frequency was generated from a microcontroller. The signal goes through the SN74LS07 IC. The 74LS07 is hex buffers and drivers that act like a Hex-Schmitt trigger to reduce ringing (oscillation before reaching stable level) of the signal and drive to the required voltage level. After that, the signal goes through the optocoupler 6N137. The 6N137 is a single channel optocoupler utilizing a highly efficient input LED coupled with an integrated optical photodiode IC detector 6N137. Its application is to provide galvanic isolation between ICs, microcontroller, and a high voltage source. It is a common practice to isolate your ICs and high voltage supply electrically, except when the IC is used for high voltage application. There is a high-speed, high-efficiency LED that transmits the signal from the input side and a photodiode IC detector at the output side to receive the signal and transmit it to the other devices. Signal was transmitted and received by light, hence the name optocoupler. This optocoupler was chosen because of its great switching characteristics. The output raise time and fall time are only 23 ns and 7 ns, respectively. The propagation delay time is at 48 ns typically and is suitable for the operating frequency of 3 MHz, where one cycle happens in around 333.33 ns.
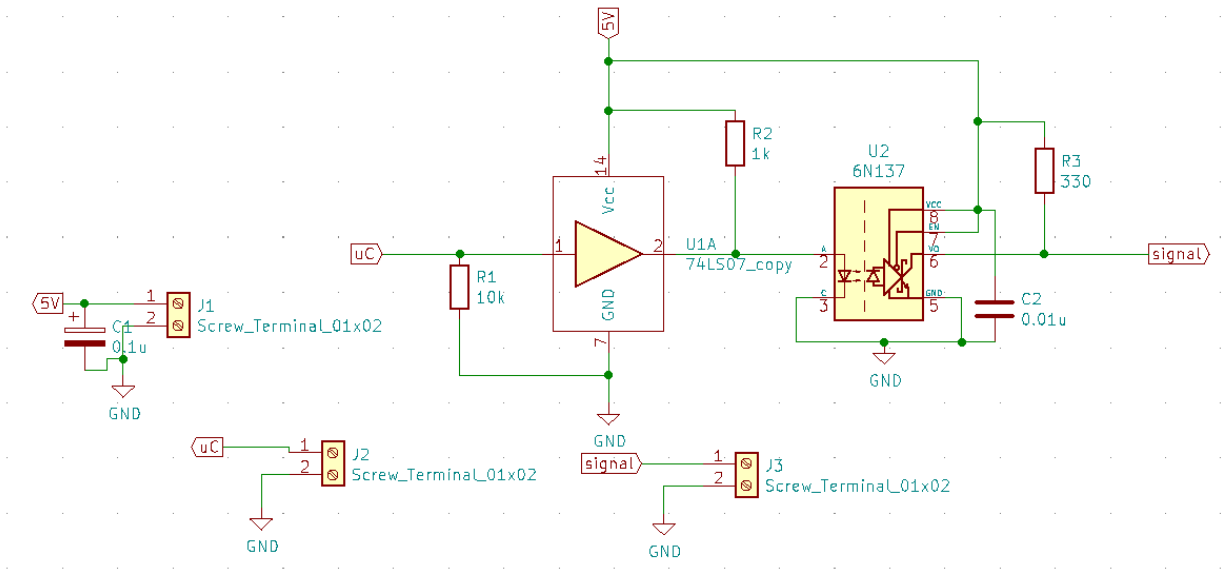
Figure 4.9 Signal Processing sub-circuit schematic

The MOSFET gate driver and resonant network circuit are shown in Figure 4.10. This sub-circuit comprises a MOSFET driver, and the remaining is the class E RF amplifier talked about in the previous section.

Unlike the bipolar transistor, MOSFET is a device driven by voltage. In the MOSFET datasheet, the gate threshold voltage V_{TH} is defined as the minimum bias voltage for produce conduction between the drain and source region, or the voltage to turn ON the MOSFET in short [35]. In gate driver design, the gate charge Q_g is considered since it is responsible for turning ON the MOSFET. In practice, there is a very small current (on the order of nanoamperes) flowing into the gate and the time to fully charge the gate could be calculated as:

$$Q_g = i_g \times t \ or \ t = \frac{Q_g}{i_g}$$

By establishing a suitable charging time for the operating frequency, one can calculate the gate current and then determine the gate resistor using:

$$R_G = \frac{V_G}{i_G} \quad\quad\quad (4.21)$$

where V_G is the drive voltage.

There are several types of gate drive circuit, including the basic drive circuit with one gate resistor, the Logic drive (logic level drive voltage), high side drives from half/full bridge, transformer drive... In this application, to simplify the process, the MOSFET driver IC TC4420 was chosen. TC4420 is a Microchip 6A high-speed MOSFET driver [36]. Its advantage is short rise and fall time (25 ns), wide input supply voltage range (4 to 18V), short delay time, and fairly simple circuit configuration.

The resonant tank network circuit is drawn and modeled with the components chosen followed by the circuit simulation results.
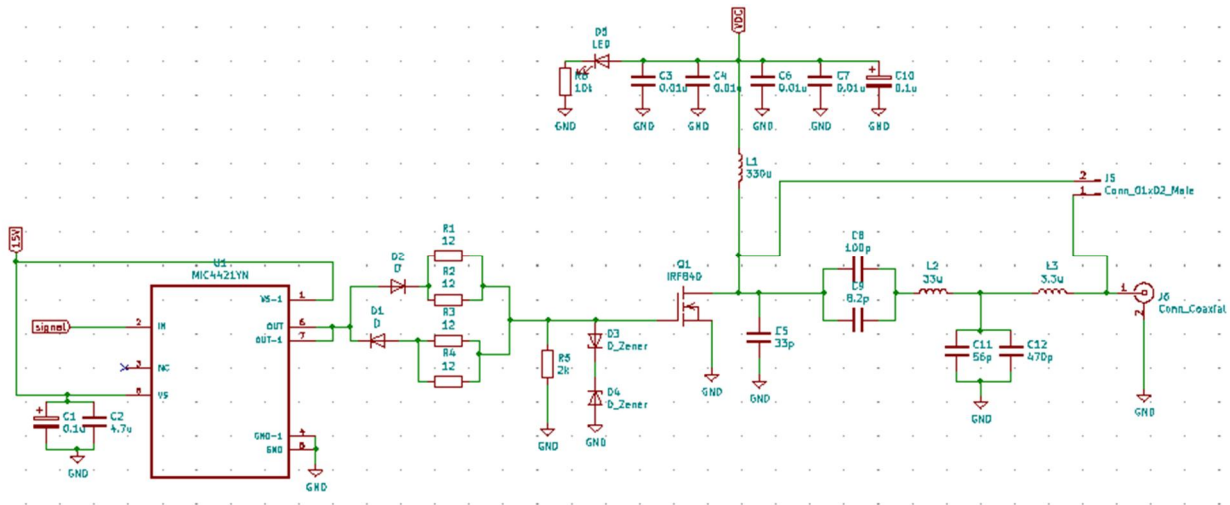

Figure 4.10 Gate driver and resonant network sub-circuit schematic

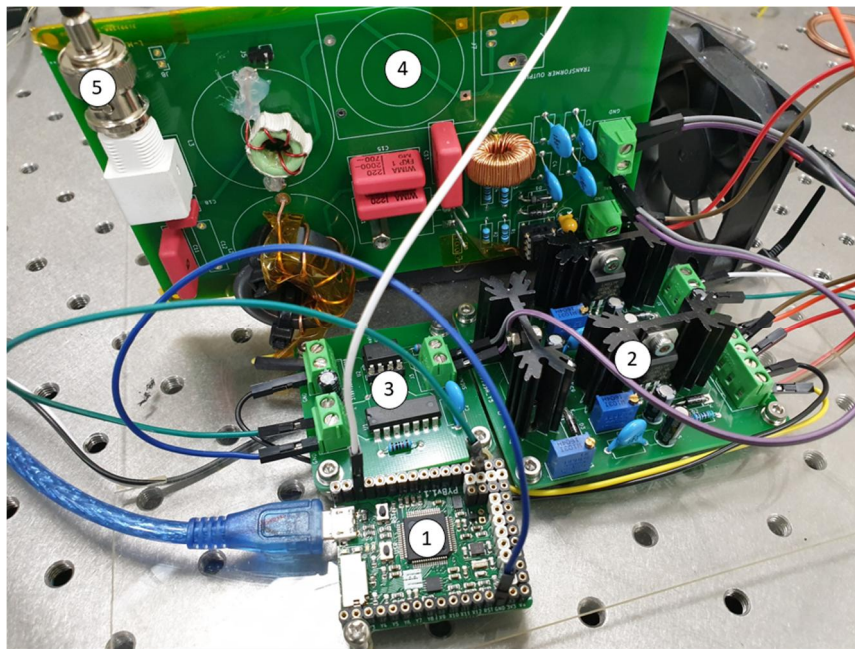The fabricated RF power amplifier is shown in Figure 4.11 below:

Figure 4.11 RF power amplifier prototype circuit. 1) Microcontroller 2) DC regulators 3)Signal processing 4) Gate driver and resonant circuit 5) RF output (BNC)

4.3 Design of L-matching network

4.3.1 Controllable L-matching network array

A 2-component L-matching network in Figure 4.12 was selected as the topology for the matching network in the iU-50 thruster. As reviewed in Chapter 2, the L-matching network could serve as a simple and effective circuit to implement in the RF power system.
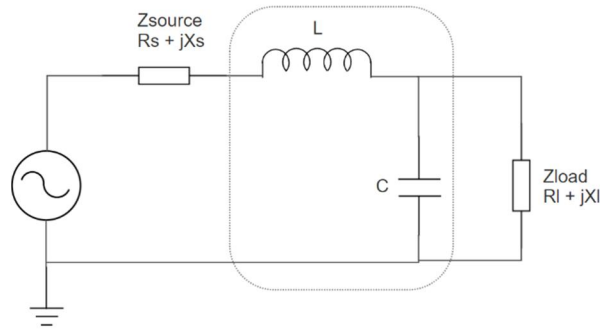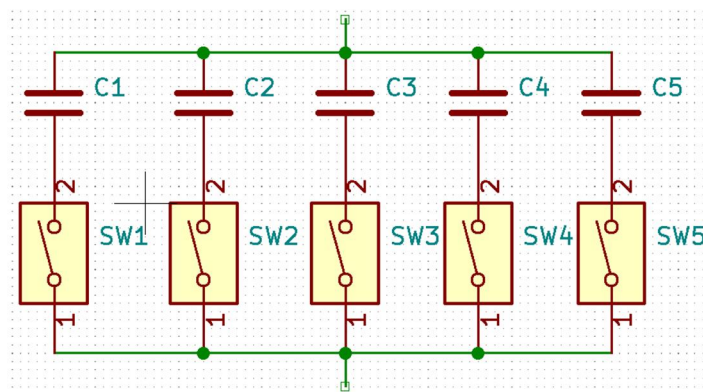
Figure 4.12 LC matching network

To implement the matching network with high power transfer efficiency, the matching network should not be at a fixed value. In the practical operation of an RF ion thruster, there are three main operating regimes:

- Idling state (no plasma).

- Transient state (starting to have plasma).

- Working state (steady-state plasma inside discharge chamber).

The matching network is focused on the working state 1 and 3 of the RF ion thruster and should guarantee maximum power transfer efficiency in both cases. To realize this condition, a digitally switched network of capacitors and inductors was utilized. Figure 4.13 illustrates the idea of the switched array of inductors and capacitors. The capacitors are connected in parallel, and the inductors are connected in series, each leg has a digitally controllable switch. When a switch is closed, the total capacitance will increase by the value of its capacitor's leg and the opposite happens for the inductor array, when a switch in the inductor array is open, the total inductance of the array will increase.
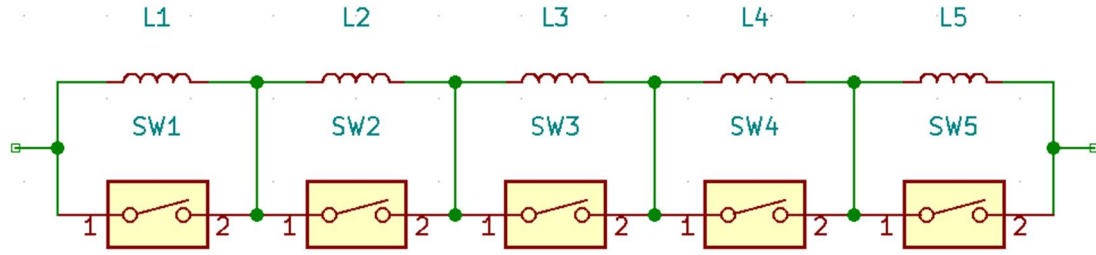
Figure 4.13 Switched array of capacitors and inductors.

A diagram of the matching network was shown in Figure 4.14. A directional coupler was placed into the line right after the source to sample the forward and reflected power and these powers were measured by RF power meter. Power data will be fed into the controller. The capacitors and inductors will be variable-type that could be digitally controlled and integrated into the satellite control system.
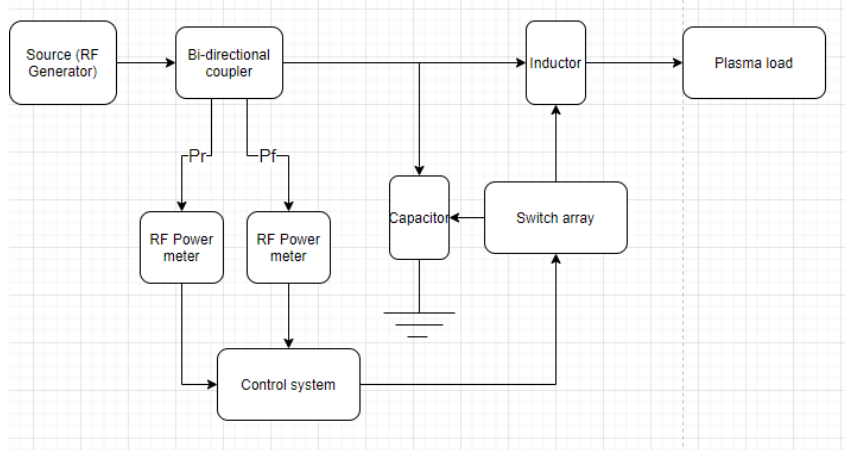

Figure 4.14 Matching network diagram

With the goal of minimizing the reflected power, a Direct search method [37] was implemented into the tuning work of the matching network. At each tuning iteration, the reflected power would be measured and checked whether it is under the threshold. If not, the values of inductors and capacitors will be adjusted by one small $\Delta L, \Delta C$ values and go to the next iteration, where the reflected power is measured again. This process keeps running until the satisfied value of reflected power is achieved. With this simple direct search method combined with a well-designed matching network, great performance of the matching network could be achieved.

4.3.2 Prototype circuit

A prototype circuit of the matching network circuit was fabricated at the AARL in the University of Ulsan. Its schematic diagram is presented in Figure 4.15. The switched array of inductors and capacitors utilized the DG411 IC to implement the digitally controllable array. DG411 is a precision monolithic quad SPST CMOS analog switch. Its high speed of switching helps to adjust the matching

network components values rapidly through a series of power relays. The input and output terminals are using BNC connections. The prototype circuit is presented in Figure 4.16.
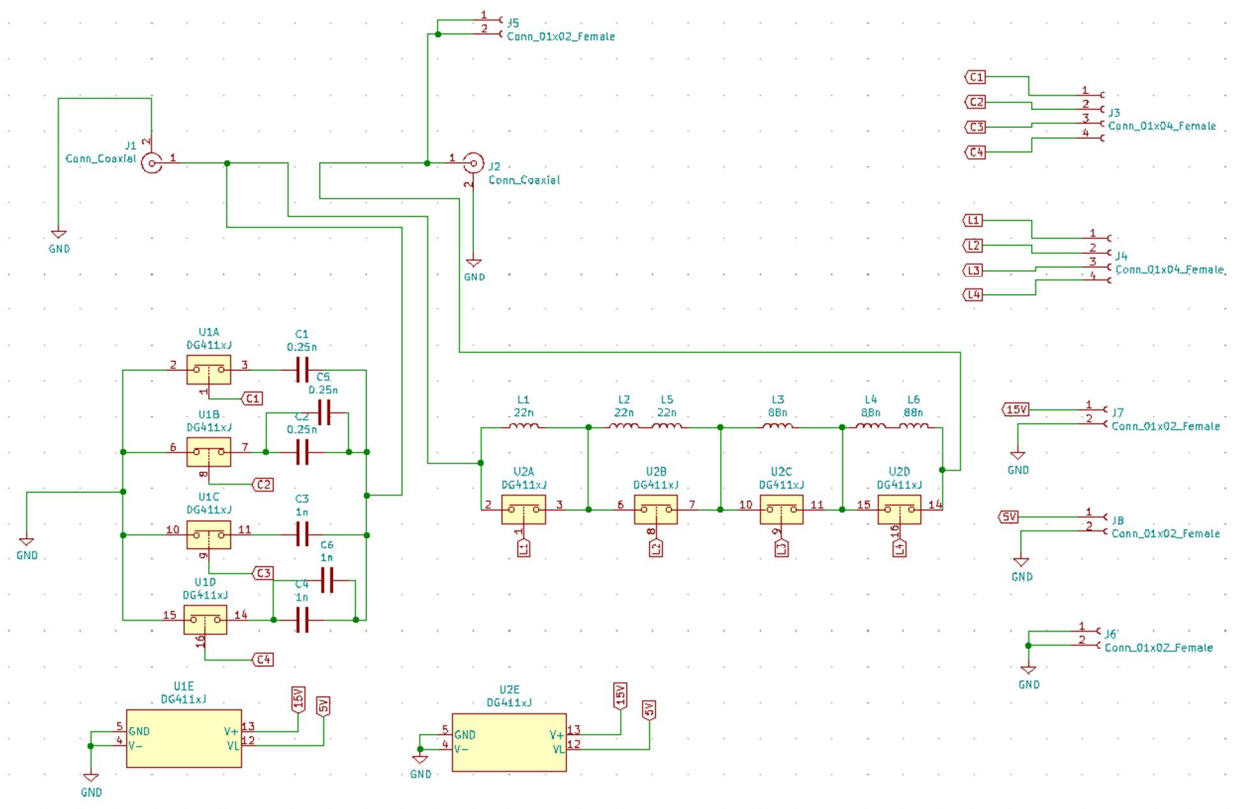
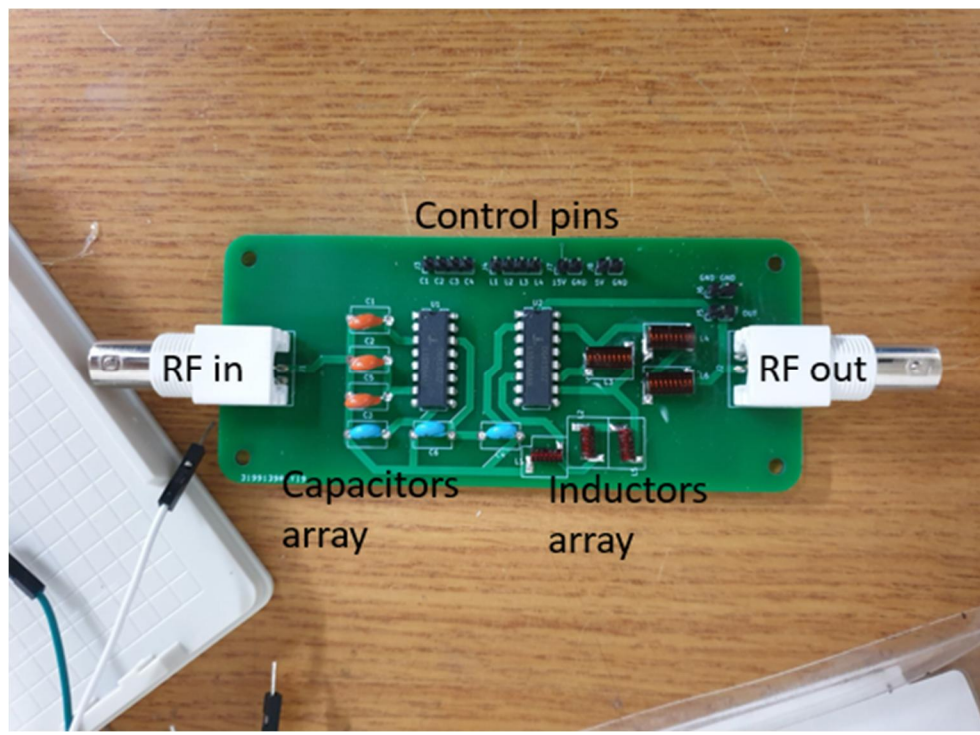

Figure 4.15 Matching network schematic

Figure 4.16 RF matching network prototype circuit

4.4 Testing procedure

The fabricated prototype circuits were put in experiments to evaluate the design of the RF power supply system for the RF ion thruster application. The testing procedure will include two parts: testing with dummy load and testing with RF ion thruster in the vacuum chamber.

4.4.1 Testing with the dummy load

The testing with dummy load procedure includes the testing of RF power amplifier with standard 50 Ω load and the testing of dummy load with resistance and inductance similar to the plasma impedance.

The 50 Ω load for testing was fabricated from two 100 Ω resistors connected in parallel. The resistors are made from cement and have a high power-rating up to 50 W, suitable for the RF power amplifier evaluation. The set-up is presented in Figure 4.17. The output signal is connected to an RF bi-directional coupler then to the load. The directional coupler is used for measuring the signal strength of the forward and reflected power. It is connected to an RF meter which will transmit the RF signal strength to the terminal of the computer. The output voltage signal waveform was measured and recorded with a high-speed oscilloscope to evaluate the RF signal.
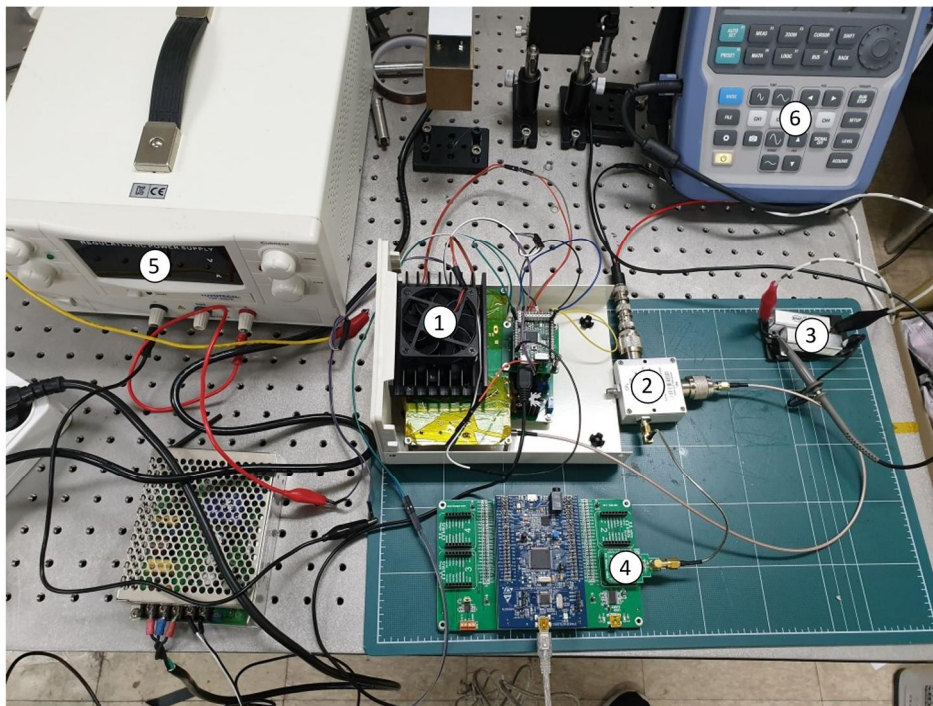

Figure 4.17 RF power amplifier dummy load test set-up 1) class E amplifier; 2) Directional coupler; 3) Dummy load; 4) RF power meter; 5) DC power supply; 6) Oscilloscope

The dummy load testing with the impedance of plasma is tested with the RF power amplifier connected to the matching network. The dummy load comprised of a resistor and an air-cored inductor,

made with specific values that were determined in the Chapter 3 prediction. The set-up for testing is presented in Figure 4.18. The same measurement procedure as in 50Ω load was carried out for this test.
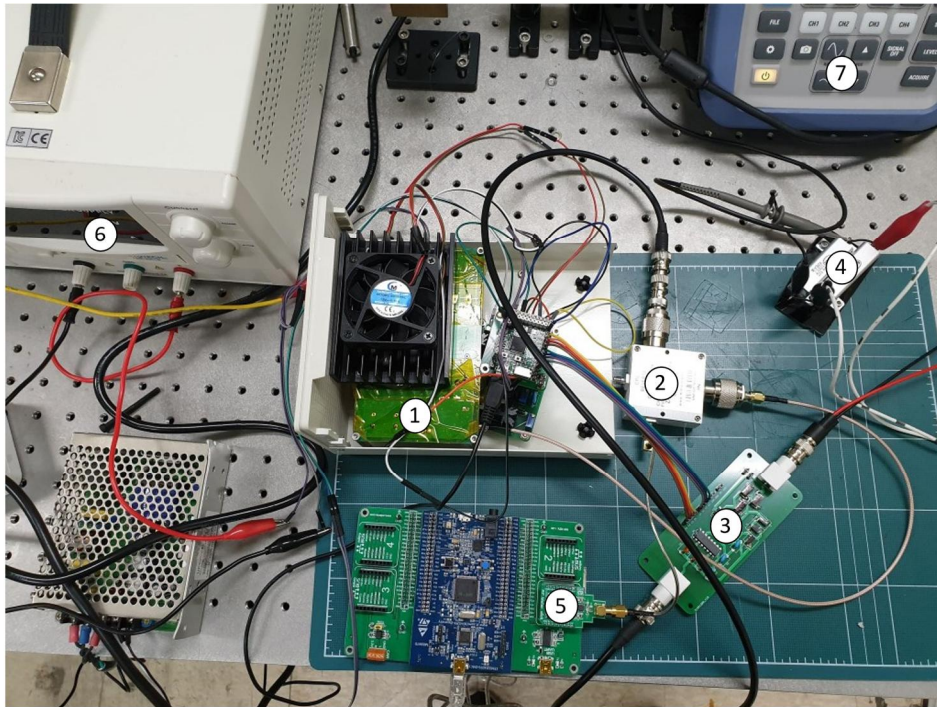

Figure 4.18 RF power amplifier with matching network dummy load test set-up 1) class E amplifier; 2) Directional coupler; 3) Matching network circuit; 4) Dummy load; 5) RF power meter; 6) DC power supply; 7) Oscilloscope

4.4.2 Testing in RF ion thruster in vacuum

The test of the RF power supply system in RF ion thruster is to evaluate the performance of the system in generating RF plasma. The experiments are carried out with the iU-50 thruster. Videos of the experiment are recorded to observe the plasma stability in the discharge chamber. Power measurements with the directional coupler are also measured to evaluate the power transfer efficiency. Figure 4.19 presents the experimental set-up for the testing of the RF power supply system in the RF ion thruster in the vacuum chamber.
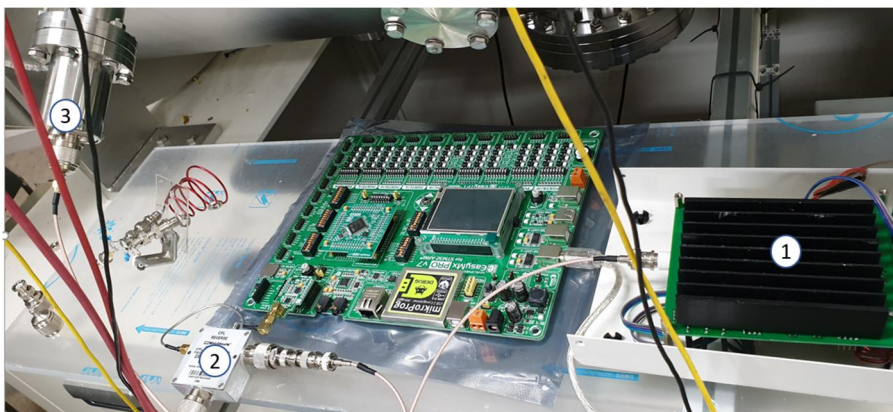
Figure 4.19 RF power supply system testing with RF ion thruster in the vacuum chamber. 1) RF generator; 2)Directional coupler; 3) Electrical feedthrough.

5   Result and discussions

5.1 Analytical model results

The RF ion thruster iU-50 discharge chamber geometrical parameters, grids system parameters, and operating conditions were put in the input of the analytical model. The output parameters involved in plasma characteristics are plasma density, plasma electron temperature and pressure versus absorbed power were shown in Figure 5.1. The plasma density shows a tendency to decrease when power increase. However, the density of plasma is always at the order of 10^{17} (m^{-3}) and the operation of the thruster could be considered as working at the high-density regime. The electron temperature increase with the power and this is in agreement with the experiment results in [38].
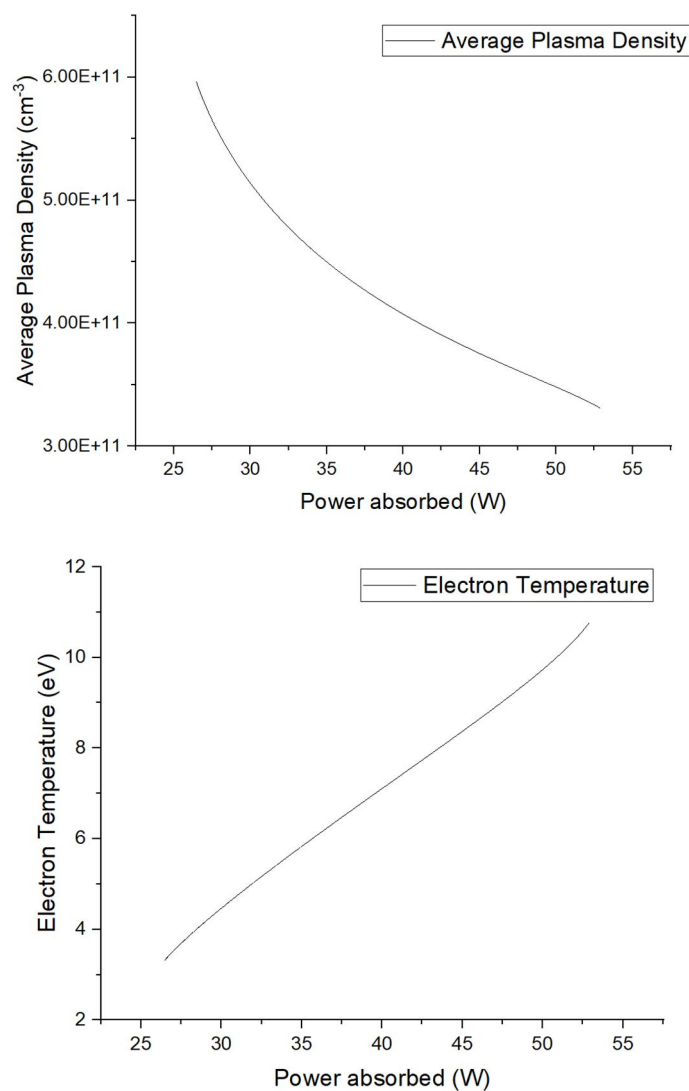

Figure 5.1 Plasma density and electron temperature vs. Power absorbed.

The parameter related to the electrical impedance of the RFIT system is the coil current. The RF current flowing in the coil tends to increase linearly with the absorbed power as observed in Figure 5.2. By obtaining the coil current and the average absorbed plasma power in the analytical model, the

electromagnetic model resistance R_{ind} could be calculated, thus the plasma resistance could be determined by adding the calculated coil to it. In Figure 5.3, the plasma resistance is plotted against the absorbed power. The plasma resistance is in the range of 10 (Ω) to 10.4 (Ω), a rather narrow span that could be utilized as the RF matching network initial guess of the RFIT load.
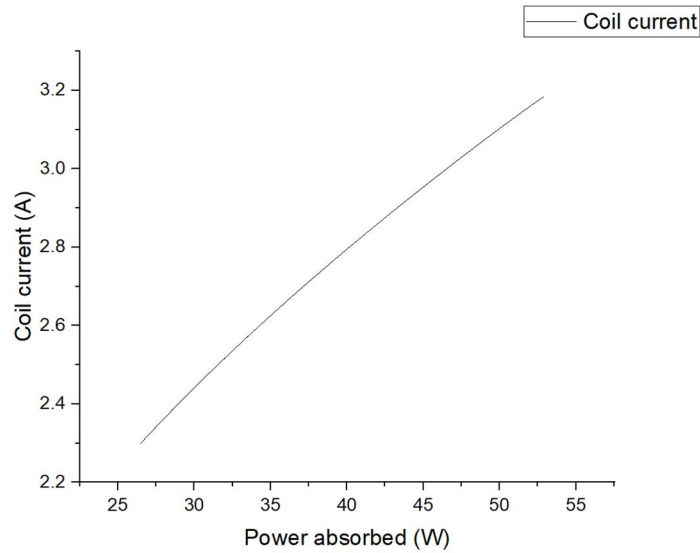

Figure 5.2 RF coil current vs. Power absorbed.
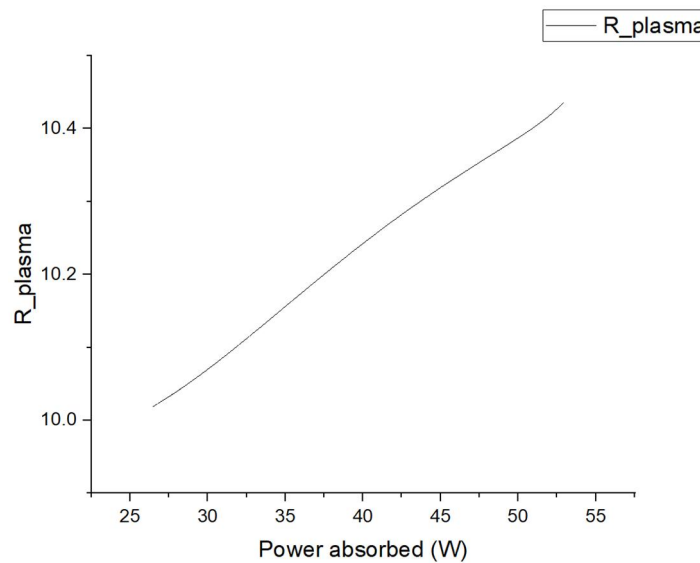
Figure 5.3 Plasma resistance vs. Power absorbed.

5.2 Plasma simulation results

The plasma simulations were computed on the laboratory server Dell PowerEdge R715. It is a 2-socket rack server offering AMD Opteron processors. The server hardware's main specifications include 16 processors, memory of 16 Gigabytes, and 160 Gigabytes of storage. This system allows heavy computational works which plasma simulation usually requires. The operating system running on this is 64-bit CentOS, a Linux OS with a graphical user interface for effortlessly working with the VizGlow

47

software. Thanks to the high specifications of the server, the complicated plasma model as described in Chapter 3 could be computed rapidly. A time-accurate simulation with 40,000 timesteps of 2.5×10^{-10} (s) would take around 38,000 (s) for computing.

<u>Simulations for standard operating conditions: RF power 50W; RF frequency 3 MHz</u>:

Figure 5.4 shows the ion density in the discharge chamber domain of the simulation at the final time of the simulation (1E-5 (s)). This simulation is set up with the working condition of RF power of 50W and 3MHz. The ion Xe+ density was distributed highly at the center of the discharge chamber with the highest concentration of 1.1E+17 ($1/m^3$) and lowest of 7.3E+15 ($1/m^3$). The area near the grid has lower density of plasma. A graph of average number density in the discharge chamber is presented in Figure 5.5. The initial density set up for the Xe+ species was 1E+16 ($1/m^3$) and in the period of 1E-5 (s), the average number density for Xe+ reach stability at around 4.3E+16 ($1/m^3$).
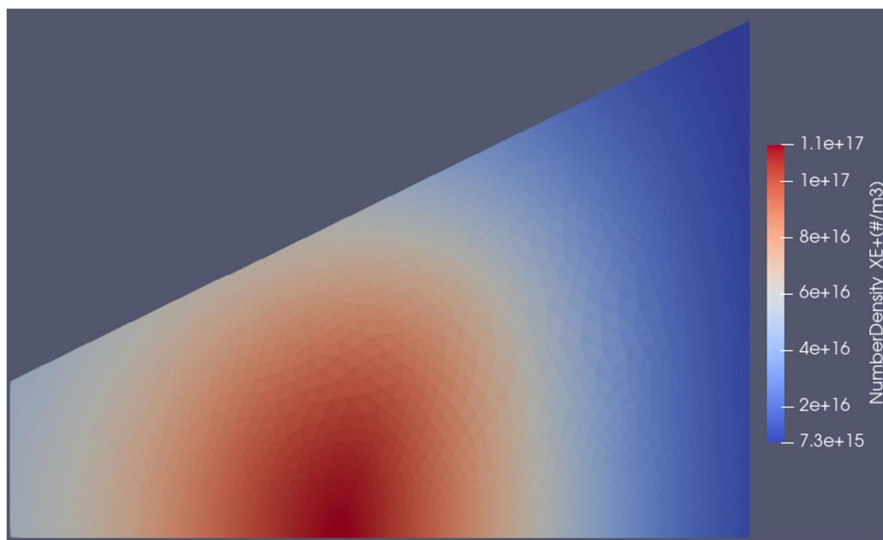

Figure 5.4 Number density of Xe+ at final timestep.
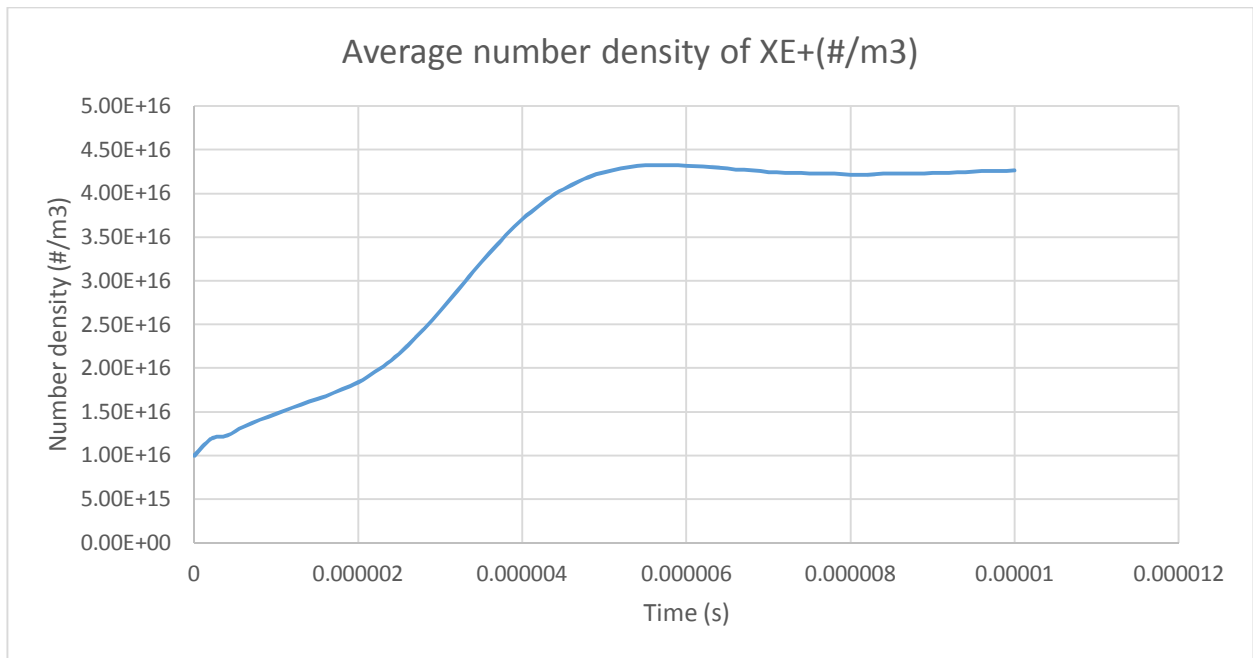
Figure 5.5 Average number density of Xe+ over time

The electron temperature of the plasma inside the discharge chamber at the final time step is shown in Figure 5.6. Its profile is distributed higher near the grid system and central area. The absorbed power profile of the plasma is presented in Figure 5.7. Most of the power absorbed in plasma is concentrated in the area near the chamber wall. The area near the central axis and around the grids absorb little power, around 1000 (W/m^3) to 10000 (W/m^3) and the lowest at 1.7E-1 (W/m^3).
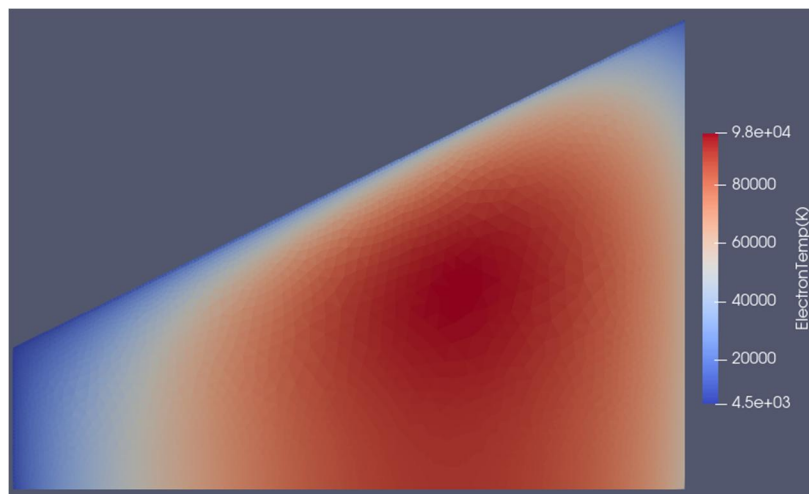
Figure 5.6 Electron temperature of the plasma in the discharge chamber
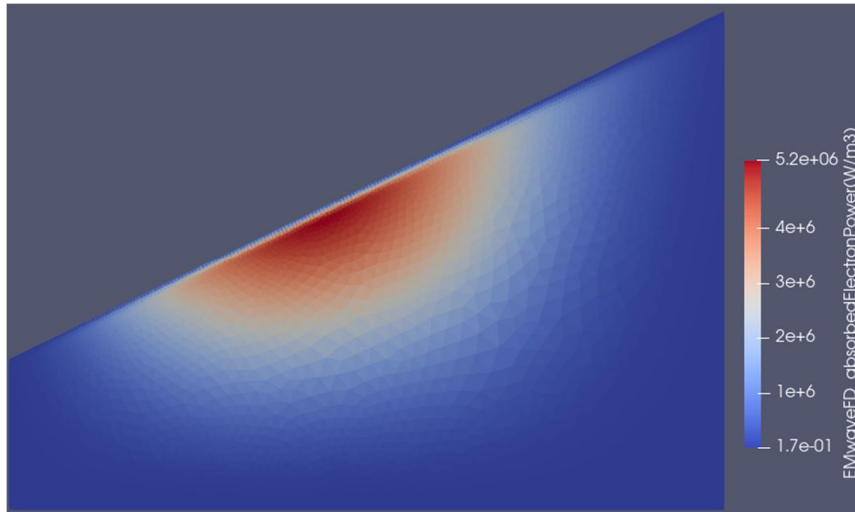
Figure 5.7 Absorbed electron power of plasma in the discharge chamber.

In the plot of the plasma number density over the middle radial length of the discharge chamber in Figure 5.8, the density is at the highest at the axis at around $10^{-7}(1/m^3)$ and decrease sharply towards the wall. The electron temperature at the middle line shown in Figure 5.9 reaches the highest value of around 90000K or about 7.7 eV. This value is in agreement with the analytical results.
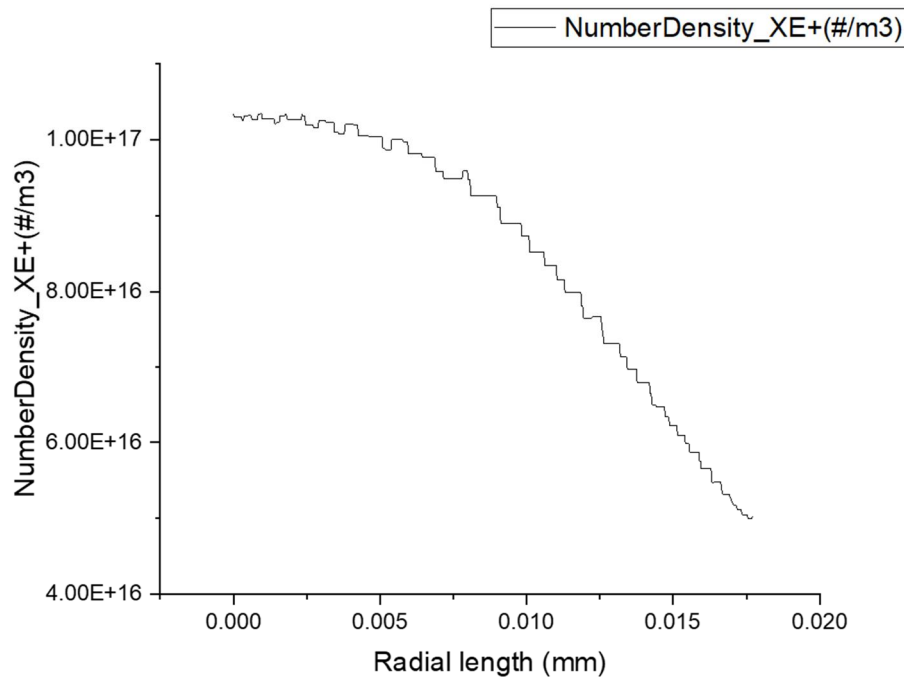
Figure 5.8 Xe+ ion density over radial length at the middle of the discharge chamber

50
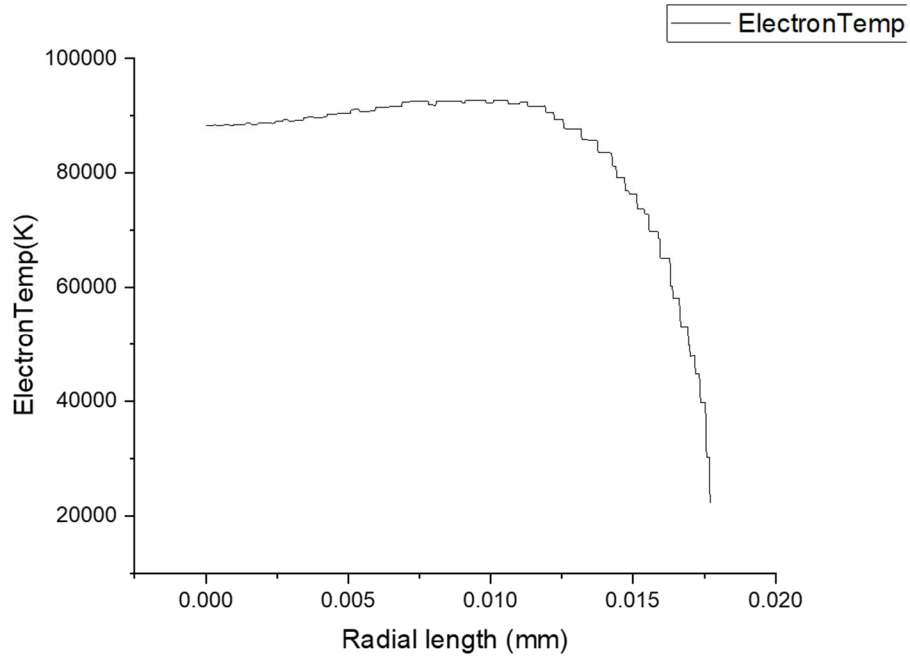
Figure 5.9 Electron temperature over the radial length of the middle line

The plasma complex conductivity of the ICP discharge in the chamber is presented in Figure 5.10. The plasma could be treated as a conductor with complex conductivity. The plasma impedance could be calculated by averaging the complex conductivity and incorporating it with the equations in [20]. The plasma resistance in different power configurations is shown in Figure 5.11. The resistance is increased with the applied power and the range is close to the analytical results.
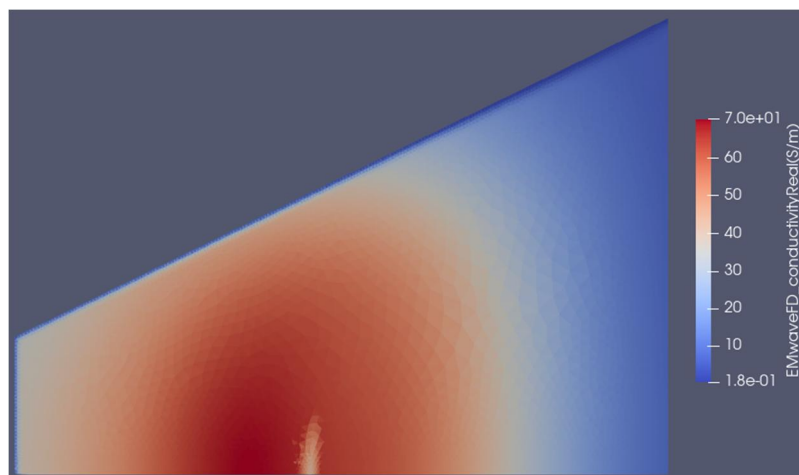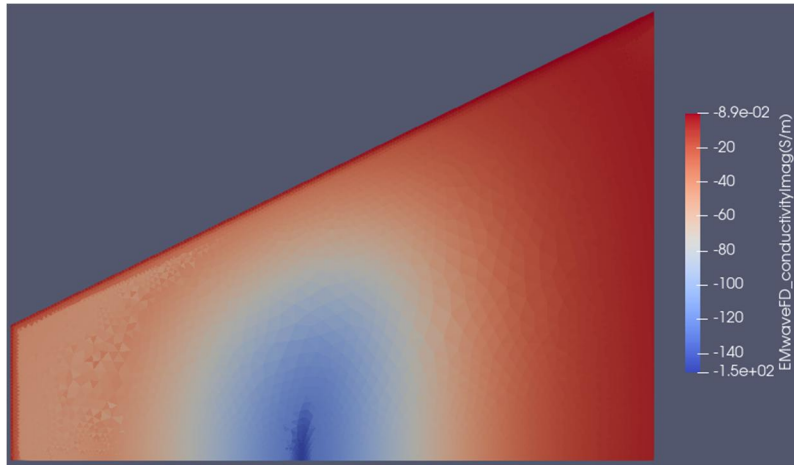
Figure 5.10 Plasma complex conductivity (Real and Imaginary value)
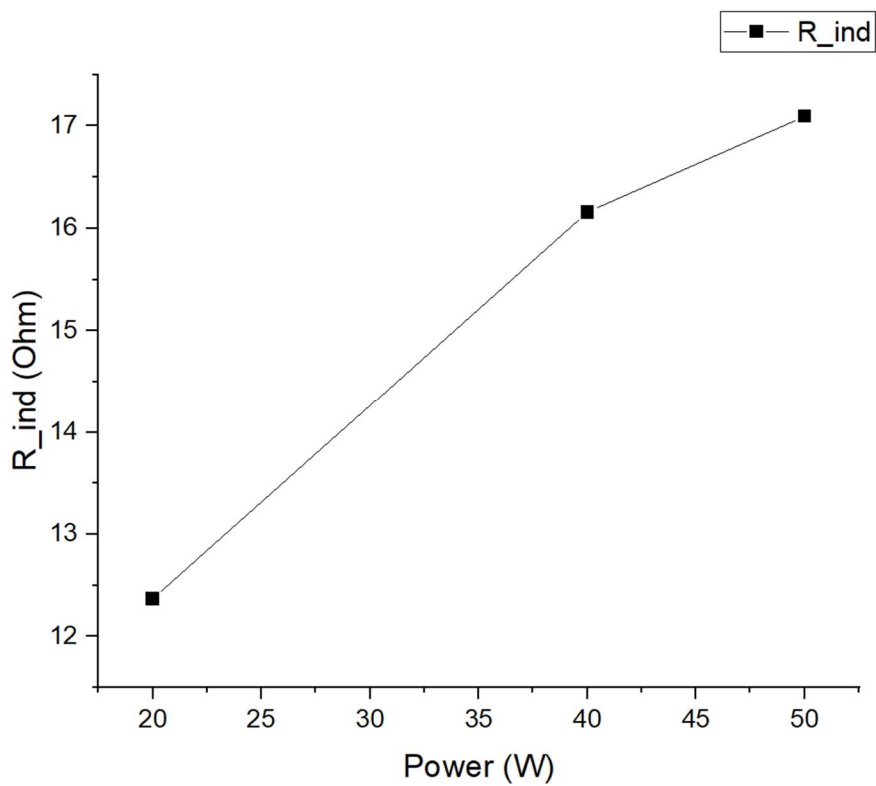
Figure 5.11 Plasma resistance in different power configurations

Simulations for different RF powers:

Simulations for two other different RF power: 20W and 40W were performed. In Figure 5.12, the number density of ion Xe+ versus time between different power configurations is graphed. At higher RF power setup 40W and 50W, the plasma's ion density reached a stable value at around 5E-6 (s) while it takes 20W configuration longer time as the number density of Xe+ ion keeps fluctuating. The final time value of Xe+ ion density is increased with higher RF power coupled to at 50W, the number density is around 4.27E+16 (m^{-3}) while this number is 3.84E+16(m^{-3}) and 2.58E+16(m^{-3}) at 40W and 20W, respectively. High-density plasma inside the discharge guarantees a better performance of the RF ion

52

thruster. The values of average plasma density are also close to the analytical model described in Chapter 3.
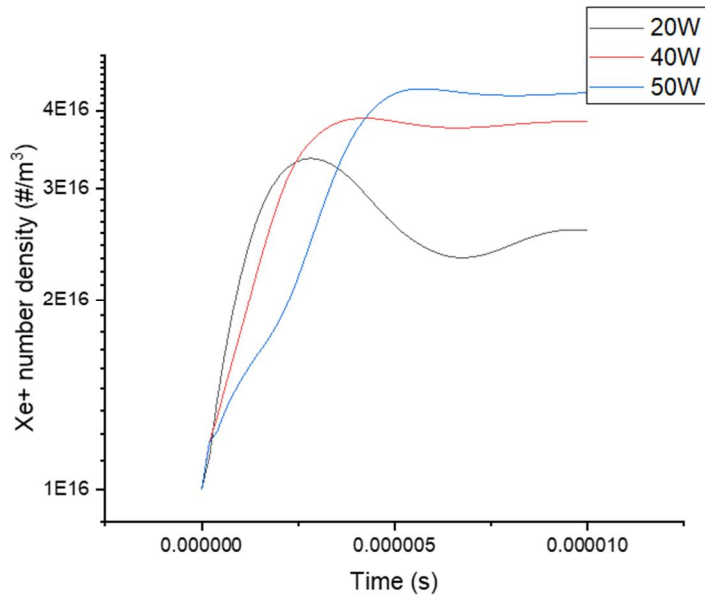
Figure 5.12 Ion number density over time of different power configurations

The electron temperature over time of different power configurations was also investigated. Figure 5.13 shows the graph of the electron temperature (K) over time. We can observe a trend where electron temperature reaches a very high value in the order of 10^5 (K) then decreases. The final time value of 20W, 40W and 50W electron temperature are 5.3E+4 (K), 5.6E+4 (K) and 5.8E+4 (K). The value of electron temperature differences between each power configuration is not much as the RF powers are relatively close. These differences agree with the experiments in literature [38], where electron power is linearly dependent on the injected microwave plasma power on the log scale, indicates that electron temperature changes slowly with power.
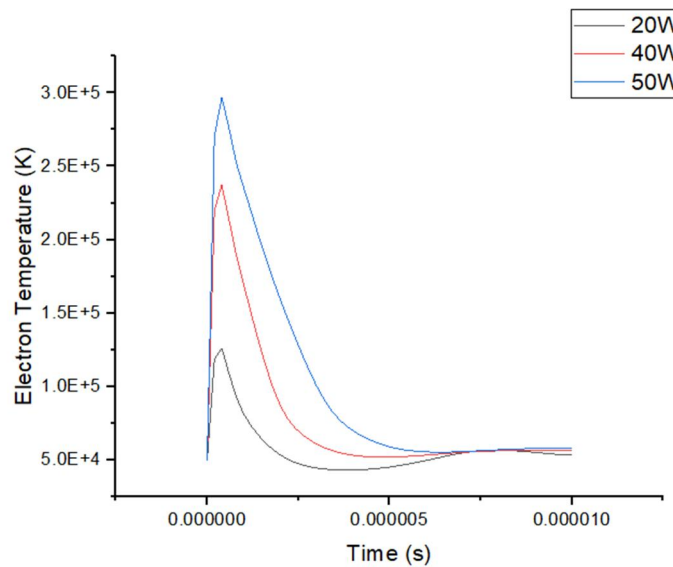
Figure 5.13 Electron temperature over time of different power configurations

Simulations for different RF frequency:

Simulations for four other frequencies of the RF power: 5, 13.56, 27.12, 51.24 MHz have been performed. In these simulations, plasma characteristics such as electron density, electron temperature do not vary significantly as can be seen in Figure 5.14. The average electron number density only decreases slightly as the frequency increases with the peak value at the 3 MHz frequency. However, the plasma complex conductivity at different frequencies can be changed significantly as showing in Figure 5.15. The magnitudes of real and imaginary values of the complex conductivity decrease as the frequency increase and as the frequency grows bigger, the magnitude decrease more slowly. As the frequency continues to increase, the complex conductivity of the plasma might reach a value that could be considered to be constant and this value should be close to zero, hence in that configuration, the plasma inside the discharge chamber might not be considered as a conductor with complex conductivity. The change in electron density and plasma conductivity also alter the calculation of the plasma resistance as in Figure 5.16.
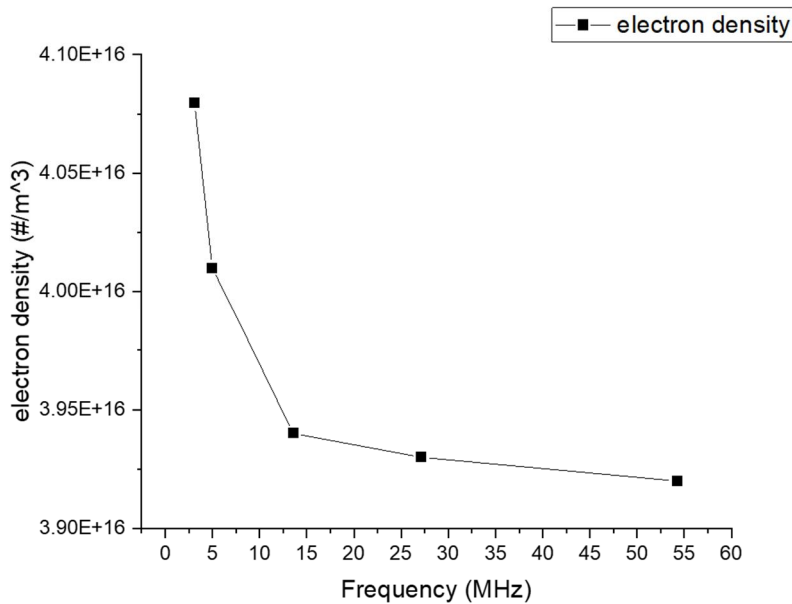
Figure 5.14 Electron density at different frequencies.
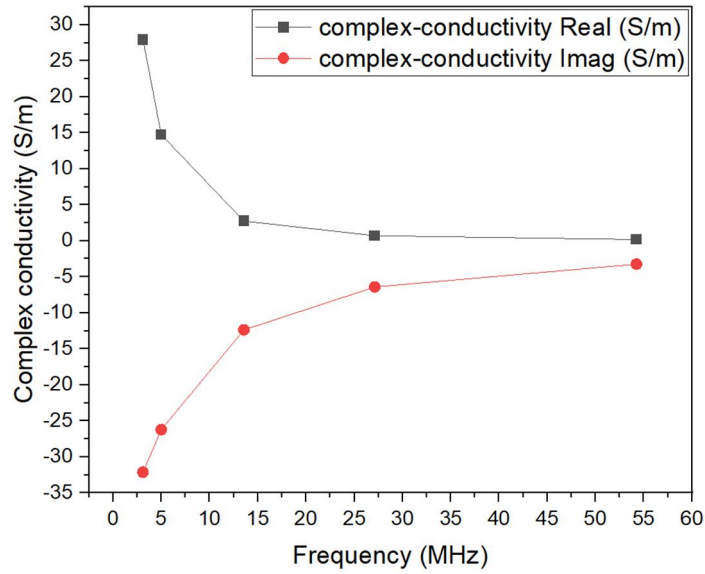
Figure 5.15 Plasma complex conductivity at different frequencies.
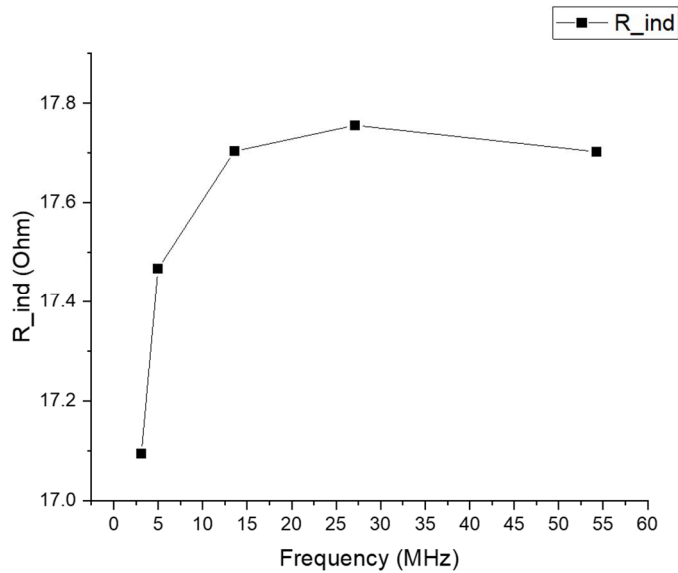
Figure 5.16 Plasma resistance at different frequencies

5.3 RF power supply prototype circuit testing

5.3.1 Dummy load tests

The testing of the RF power amplifier was carried out with the load 50 Ω. The voltage of the gate junction of the MOSFET has been recorded by the oscilloscope in Figure 5.17. The gate drive voltage has achieved the required frequency of 3MHz, drive level higher than the threshold voltage, and duty-cycle of approximately 50%. This proves the normal operation of the gate driver circuit and the design of gate resistance.
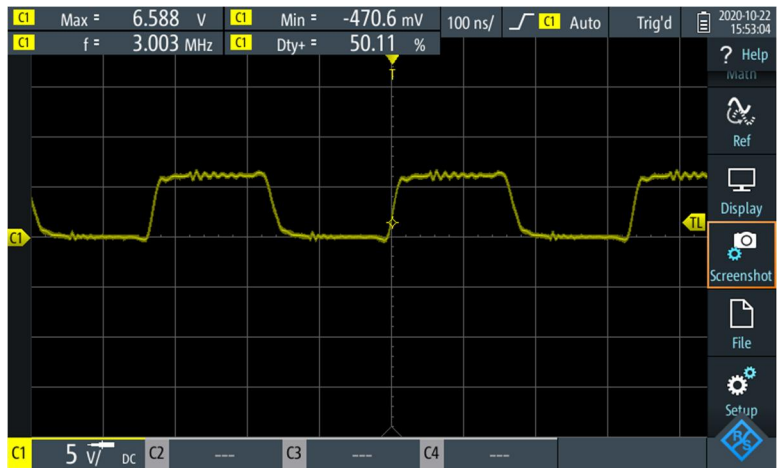
Figure 5.17 Gate driver voltage capture

Figure 5.18 shows the output voltage waveform of the RF amplifier at different input power. It could be seen that the voltage waveform has achieved a sinusoidal waveform and duty cycle of 50% at the required frequency of 3MHz. The output forward power data has been measured with an RF power meter connected to the directional coupler. Table 5.1 shows the power conversion data of the RF power amplifier.

(a)
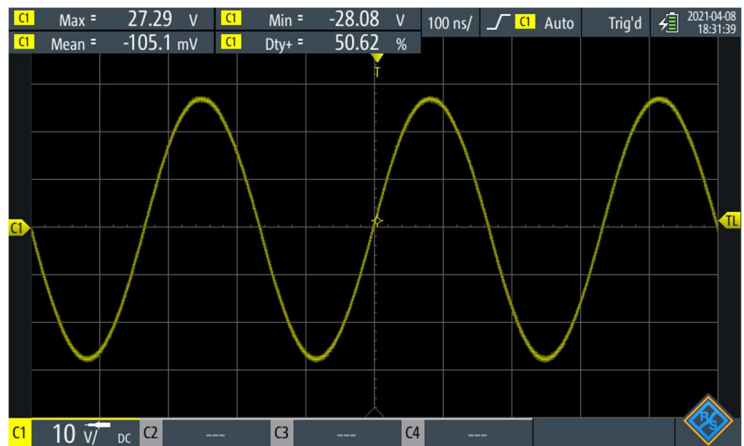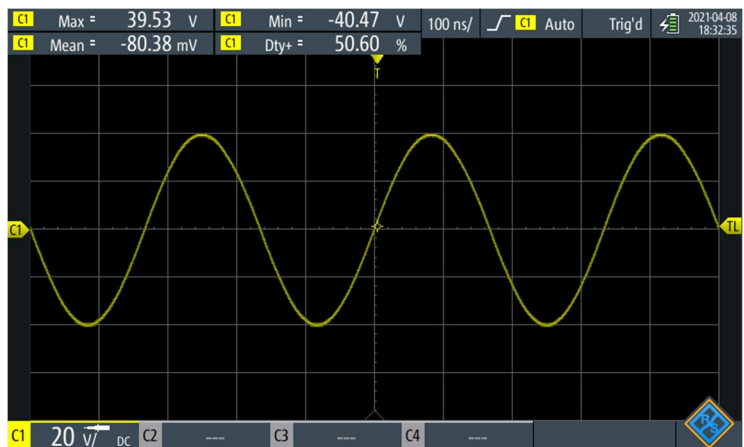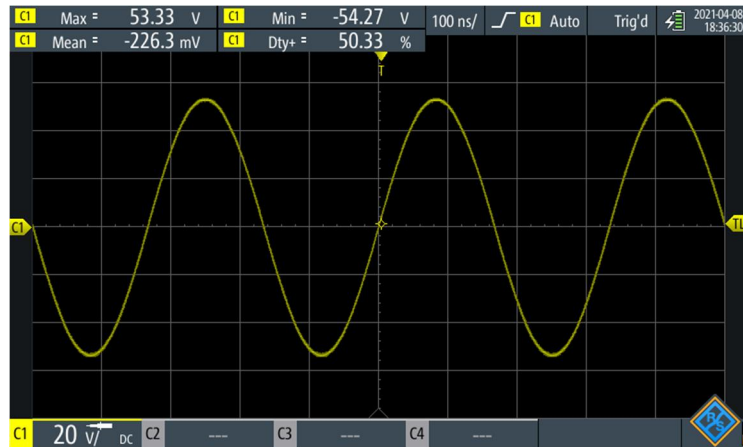
(c)
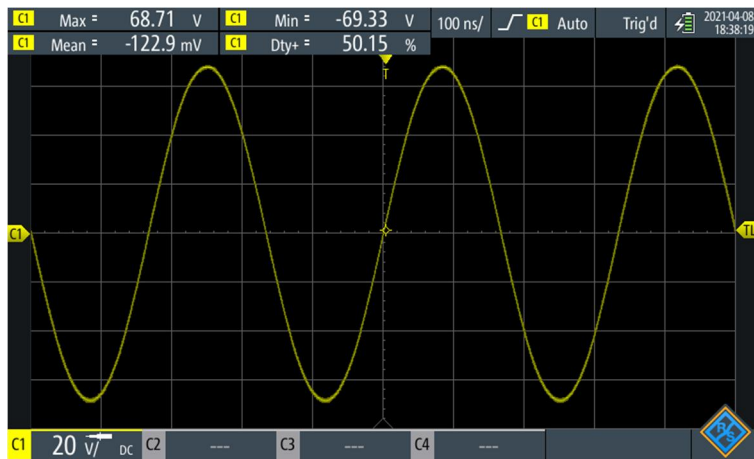
(d)

Figure 5.18 RF power amplifier output voltage at input power of: a) 10W; b) 20W; c) 30W; d) 50W

The soft-switching operation of the RF amplifier was achieved to a certain extent. In Figure 5.19, the waveforms at the drain and the switching voltage waveform are presented. The drain voltage waveform shape in green was altered to reach zero at the turn ON point by tuning the resonant network components and the shunt capacitor. As it reaches zero at this point, the power loss in the switching components was minimized, hence increasing the overall efficiency of the RF power supply system.

Figure 5.19 Drain voltage (green) and gate voltage (yellow) of the RF amplifier.

Table 5.1 Power conversion of RF amplifier

DC supply power (W)	RF output power (W)	Efficiency
25	21.1	84%
35	28.3	80.8%
45	37.3	83%
58	49.1	85%

The power conversion has been recorded in Table 5.1. The class-E power amplifier prototype circuit has achieved 85% power conversion efficiency to produce 50W output power. It is lower than theoretical calculation but still at an acceptable level since the direction has decreased the reading power due to its coupling. The peak-to-peak voltage is close to the voltage level in simulation with ideal components.

5.2.2 Vacuum testing with RF ion thruster

The RF power supply system had shown the potential to generate plasma inside the RF ion thruster as can be seen in Figure 5.20. The voltage waveform at the output of the RF power amplifier is recorded in Figure 5.21. The plasma inside the discharge chamber can be ignited and sustained for around 10 seconds. This is due to some of the faults with the old engine model and the electrical leaking in the vacuum chamber. The power loss due to heating in resonant inductor has been spotted, thus making the operation of the RF power supply system not very stable. Further testing with the new design of the RF ion thruster will be made to test the ability to generate plasma of the RF power supply system.

Figure 5.20 Plasma inside RF ion thruster (test in the vacuum chamber)

Figure 5.21 Voltage output waveform (test with the thruster inside the vacuum chamber)

6 Conclusion and future developments

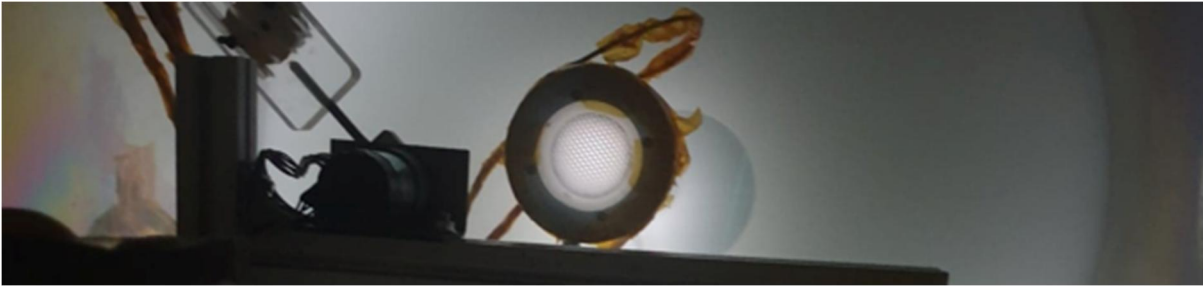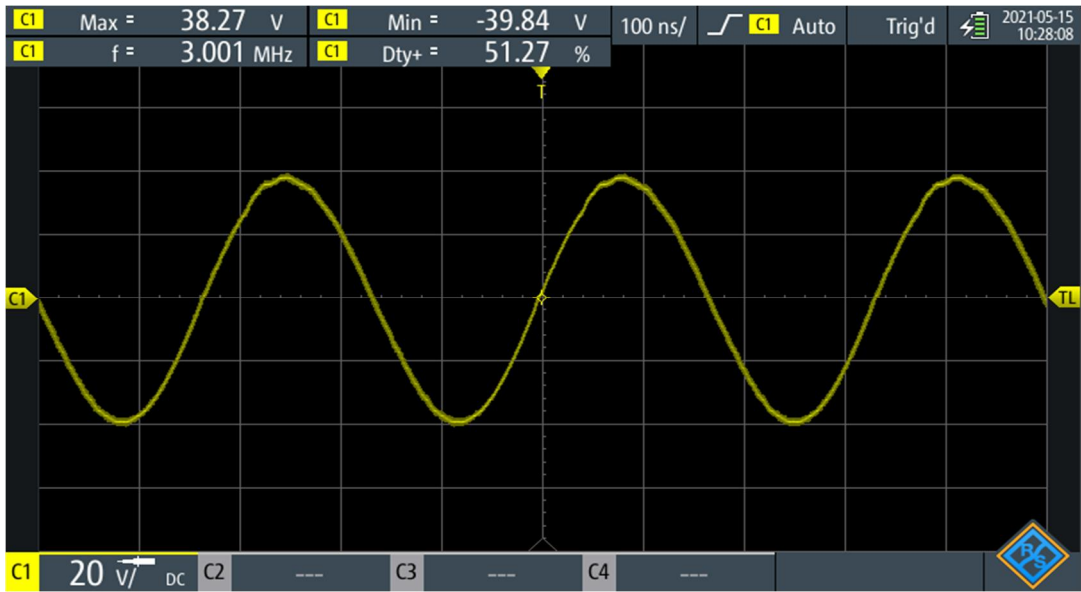In this thesis, the development process of an RF Generator system for small RF Ion Thrusters based on class E RF power amplifier and L-matching network and the simulation-based investigation of the plasma in the discharge chamber of the RF ion thruster have been presented. Power loss in the RF Generation process for RF Ion Thruster plasma, including switching loss in RF amplifier and mismatch loss due to varying plasma impedance could be minimized by utilizing the ZVS method and a tunable matching network. By using the transformer model with a 0-D analytical model, we can approximately predict the thruster load impedance in normal working conditions and enhance the impedance matching network by choosing an appropriate initial point.

Plasma simulation results have shown the characteristics of the discharge chamber's plasma in the predetermined operating conditions of the RF ion thruster. The ICP discharge is in a high density, low-pressure regime and has sufficient plasma density for the operation of the thruster. The plasma complex conductivity was numerically computed, and the electrical resistance of the plasma was estimated. By changing the power and frequency of the applied RF current to the coil, we can see the change in plasma characteristics. The plasma density increases with the power and decreases slightly when the frequency increases. The plasma resistance increases with the power and also with the frequency. The value of plasma resistance is changing in the range of 10 Ω to 20 Ω and could be used as an initial point for tuning the RF matching network.

Simulation and experimental studies of the prototype circuit have demonstrated the efficiency of the class-E power amplifier in RF generation for ICP plasma. The ZVS method was applied and switching loss was decreased, thus improve thermal behaviors and stability of the circuit. The testing with RF ion thruster in the vacuum chamber shows problems with prototype circuit components and some slight mismatch of the RF matching network. This should be set right by carefully designing and selecting components of the circuit.

Further developments to this project could be made to improve the current limitations. The efficiency of the RF Generation for RF Ion Thruster could be further increased by integrating an effective impedance auto-matching scheme like dual-frequency tuning into the existing matching network. Thermal optimization and enhanced casing could be utilized to improve the performance and protection of RFG in outer space working conditions. This developed RF Generation system is implemented in a particular condition for our RF Ion Thruster lab model. However, the concept could be utilized for a wide range of power and frequency of RF Ion Thruster, allowing more control for thruster in satellites.

References

[1] D. M. Goebel and I. Katz, "Fundamentals of Electric Propulsion: Ion and Hall Thrusters," *Fundam. Electr. Propuls. Ion Hall Thrusters*, pp. 1–507, 2008, doi: 10.1002/9780470436448.

[2] R. Killinger, R. Kukies, M. Surauer, A. Tomasetto, and L. Van Holtz, "Artemis orbit raising inflight experience with ION propulsion," *Acta Astronaut.*, vol. 53, no. 4–10, pp. 607–621, 2003, doi: 10.1016/S0094-5765(03)80022-X.

[3] D. Manzella, "Low Cost Electric Propulsion Thruster for Deep Space Robotic Missions."

[4] R. H. Goddard, "The Robert H . Goddard Papers."

[5] R. J. Cybulski, D. M. Shellhammer, R. R. Lovell, E. J. Domino, and J. T. Kotnik, "Results from SERT I Ion Rocket Flight Test," 1965.

[6] H. W. Loeb *et al.*, "Forty Years of Giessen EP-Activities and the Recent RIT-Microthruster Development," *Proc. Int. Electr. Propuls. Conf. 2005*, pp. 1–11, 2005.

[7] H. J. Leiter, R. Killinger, H. Bassner, J. Mueller, and R. Kukies, "Development of the Radio Frequeny Ion Thruster RIT XT – A Status Report," *27th Int. Electr. Propuls. Conf.*, pp. 1–8, 2001, [Online]. Available: http://erps.spacegrant.org/uploads/images/images/iepc_articledownload_1988-2007/2001index/104_4.pdf.

[8] M. Tsay, J. Frongillo, J. Model, J. Zwahlen, and L. Paritsky, "Flight Development of Iodine BIT-3 RF Ion Propulsion System for SLS EM-1 CubeSats," *Proc. AIAA/USU Conf. Small Satell.*, no. August, pp. 6–11, 2016.

[9] M. Intelligence, "GAN RF SEMICONDUCTOR DEVICES MARKET 2018," 2018, [Online]. Available: https://www.mordorintelligence.com/industry-reports/gan-rf-semiconductor-devices-market.

[10] J. SIMON, U. PROBST, and P. J. KLAR, "Development of a Radio-Frequency Generator for RF Ion Thrusters," *Trans. Japan Soc. Aeronaut. Sp. Sci. Aerosp. Technol. Japan*, vol. 14, no. ists30, p. Pb_33-Pb_39, 2016, doi: 10.2322/tastj.14.pb_33.

[11] A. Surminskii, R. Ayupov, Y. Kharlan, R. Rakhimov, and A. Systems, "Development of a compact high efficiency RF generator for inductive coupled plasma sources.," *Iepc 2019*, no. September, pp. 1–10, 2019.

[12] K. Takahashi, K. Hanaoka, and A. Ando, "Fast and Automatic Control of a Frequency-Tuned Radiofrequency Plasma Source," *Front. Phys.*, vol. 7, no. January, pp. 1–8, 2020, doi: 10.3389/fphy.2019.00227.

[13]   M. Tsay, J. Frongillo, K. Hohman, and B. K. Malphrus, "LunarCube: A Deep Space 6U CubeSat with Mission Enabling Ion Propulsion Technology," *29th Annu. AIAA/USU Small Satell. Conf.*, pp. SSC15-XI–1, 2015.

[14]   Q. T. D. Pham and J. Shin, "Better Prediction of the Performance of a Radio-frequency Ion Thruster," *J. Korean Phys. Soc.*, vol. 76, no. 2, pp. 137–144, 2020, doi: 10.3938/jkps.76.137.

[15]   J. Liang, *Chinese Siege Warfare: Mechanical Artillery & Siege Weapons of Antiquity*. 2006.

[16]   M. J. L. Turner, *Rocket and Spacecraft Propulsion Principles, Practice and New Developments (Third Edition)*, vol. Third edit. 2009.

[17]   A. R. Tummala and A. Dutta, "An overview of Cube-Satellite propulsion technologies and trends," *Aerospace*, vol. 4, no. 4, pp. 1–30, 2017, doi: 10.3390/aerospace4040058.

[18]   R. Walther, J. Geisel, and H. W. Loeb, "Scaling laws of RIT," *AIAA Int. Electr. Propuls. Conf.*, 1975.

[19]   R. B. Piejak, V. A. Godyak, and B. M. Alexandrovich, "A simple analysis of an inductive RF discharge," *Plasma Sources Sci. Technol.*, vol. 1, no. 3, pp. 179–186, 1992, doi: 10.1088/0963-0252/1/3/006.

[20]   P. Chabert and N. Braithwaite, *PHYSICS OF RADIO-FREQUENCY PLASMAS*. 2011.

[21]   M. Tsay, J. Frongillo, J. Model, J. Zwahlen, and L. Paritsky, "Maturation of iodine-fueled BIT-3 RF ion thruster and RF neutralizer," *52nd AIAA/SAE/ASEE Jt. Propuls. Conf. 2016*, pp. 1–11, 2016, doi: 10.2514/6.2016-4544.

[22]   K. Holste *et al.*, "Performance of an iodine-fueled radio-frequency ion-thruster," *Eur. Phys. J. D*, vol. 72, no. 1, pp. 1–7, 2018, doi: 10.1140/epjd/e2017-80498-5.

[23]   T. A. Trudel, S. G. Bilen, and M. M. Micci, "Design and performance testing of a 1-cm miniature radio-frequency ion thruster," *31st Int. Electr. Propuls. Conf.*, pp. 20–25, 2009.

[24]   B. Yavuz, E. Turkoz, and M. Celik, "Prototype design and manufacturing method of an 8 cm diameter RF ion thruster," *RAST 2013 - Proc. 6th Int. Conf. Recent Adv. Sp. Technol.*, pp. 619–624, 2013, doi: 10.1109/RAST.2013.6581285.

[25]   B. N. O. Sokal, "Class-E RF Power Amplifiers," *Notes*, vol. 204, no. 204, pp. 9–20, 2001, [Online]. Available: http://scholar.google.com/scholar?hl=en&btnG=Search&q=intitle:Class-E+RF+Power+Amplifiers#0.

[26]   M. K. Kazimierczuk, *RF Power Amplifiers*. 2015.

[27]   C. BOWICK, J. BLYLER, and C. AJLUNI, *RF Circuit Design*. 2008.

[28]   Q. T. D. Pham, "Design of an RF ion thruster," University of Ulsan, 2019.

[29]   M. SANGREGORIO, K. XIE, N. WANG, N. GUO, and Z. ZHANG, "Ion engine grids: Function, main parameters, issues, configurations, geometries, materials and fabrication methods," *Chinese J. Aeronaut.*, vol. 31, no. 8, pp. 1635–1649, 2018, doi: 10.1016/j.cja.2018.06.005.

[30]   EsgeeTechnologies, "Plasma Modeling Software for Multi-Dimensional Simulations of Non-Equilibrium Glow Discharge Systems User Manual Version 2.4." 2021.

[31]   EsgeeTechnologies, "Vizglow product." https://esgeetech.com/products/vizglow-plasma-modeling/.

[32]   W. J. McCalla, *Fundamentals of Computer-Aided Circuit Simulation*. Springer, Boston, MA, 1988.

[33]   VISHAY, "IRF840, SiHF840 datasheet." https://www.vishay.com/docs/91070/sihf840.pdf.

[34]   TexasInstruments, "LM317 3-Terminal Adjustable Regulator datasheet." https://www.ti.com/lit/ds/symlink/lm317.pdf?ts=1618450547659&ref_url=https%253A%252F%252Fwww.google.com%252F.

[35]   Toshiba, "MOSFET Gate Drive Circuit Application Note," 2018. [Online]. Available: toshiba.semicon-storage.com › info › docget%0A.

[36]   Microchip, "TC4420/TC4429 datasheet." https://ww1.microchip.com/downloads/en/DeviceDoc/21419D.pdf.

[37]   R. O. Chunlei Zhang, *Extremum-Seeking Control and Applications_ A Numerical Optimization-Based Approach*, vol. 4, no. 1. 2012.

[38]   J. Camparo and G. Fathi, "Effects of rf power on electron density and temperature, neutral temperature, and Te fluctuations in an inductively coupled plasma," *J. Appl. Phys.*, vol. 105, no. 10, 2009, doi: 10.1063/1.3126488.

Appendix: Detailed RF power amplifier design calculations

Design process of the circuit:

Calculate optimum full-load resistance:

$$R = \frac{8}{\pi^2 + 4} \frac{V_I^2}{P_O} = 0.5768 \times \frac{100^2}{50} = 115.36 \, \Omega$$

DC resistance of the amplifier:

$$R_{DC} = \frac{\pi^2 + 4}{8} R = 1.7337 \times 115.36 = 200 \, \Omega$$

Amplitude of the output voltage:

$$V_{Rm} = \frac{4}{\sqrt{\pi^2 + 4}} V_I = 1.074 \times 100 = 107.4 \, V$$

Maximum voltage across switch and the shunt capacitor C1:

$$V_{SM} = V_{C1m} = 3.562 V_I = 3.562 \times 100 = 356.2$$

Assuming amplifier efficiency $\eta = 0.9$ →calculate DC input power:

$$P_I = \frac{P_O}{\eta} = \frac{50}{0.9} = 55.55 \, W$$

Hence the DC input current:

$$I_I = \frac{P_I}{V_I} = \frac{55.55}{100} = 0.5555 (A)$$

Maximum switch current is:

$$I_{SM} = \left(\frac{\sqrt{\pi^2 + 4}}{2} + 1 \right) I_I = 2.862 \times 0.5555 = 1.59 \, A$$

The amplitude of the current through the resonant circuit:

$$I_m = \frac{\sqrt{\pi^2 + 4}}{2} I_I = 1.8621 \times 0.5555 = 1.0345 \, A$$

Assume $Q_L = 7$. Calculate the components of the load network.

$$L = \frac{Q_L R}{\omega} = 7 \times 115.36/(2\pi \times 3 \times 10^6) = 42.84 \mu H$$

$$C = \frac{1}{\omega R \left(Q_L - \frac{\pi(\pi^2 - 4)}{16} \right)} = \frac{1}{2\pi \times 3 \times 10^6 \times 115.36 \times (7 - 1.1525)} = 78.64 \, pF$$

$$C_1 = \frac{8}{\pi(\pi^2 + 4)\omega R} = \frac{8}{2\pi^2(\pi^2 + 4) \times 3 \times 10^6 \times 115.36} = 84.43 \, pF$$

Assume MOSFET output capacitance be $C_O = 34.43 \, pF$. The external shunt capacitance is:

$$C_{1ext} = C1 - C_O = 84.43 - 34.43 = 50 \, pF$$

Pick $C_{1ext} = 50pF/400V$

The peak voltages across the resonant capacitor C and peak voltage across the inductor L are:

$$V_{Cm} = \frac{I_m}{\omega C} = \frac{1.0345}{2\pi \times 3 \times 10^6 \times 78.64 \times 10^{-12}} = 697.89 \, V$$

$$V_{Lm} = \omega L I_m = 2\pi \times 3 \times 10^6 \times 42.84 \times 10^{-6} \times 1.0345 = 835.37 \, V$$

Pick $C = 80pF/700V$.

To keep the current ripple in the choke inductor below 10%, full-load DC input current I_I, the value of choke inductance must be greater than:

$$L_f = 2\left(\frac{\pi^2}{4} + 1\right)\frac{R}{f} = 7 \times \frac{115.36}{3 \times 10^6} = 269.1\mu H$$

The peak voltage across the RFC is:

$$V_{Lfm} = V_{SM} - V_I = 356.2 - 100 = 256.2 \, V$$

Assume that the DC ESR of the choke L_f is $r_f = 0.15 \, \Omega$. The power loss in r_f is:

$$P_{rLf} = r_{Lf}I_I^2 = 0.15 \times 0.555^2 = 0.0463 \, W$$

The RMS value of the switch current is:

$$I_{Srms} = \frac{I_I\sqrt{\pi^2 + 28}}{4} = 0.5555 \times 1.5385 = 0.854 \, A$$

Select the MOSFET C3M0280090D which has: $V_{DSS} = 900V$ (maximum voltage can be applied between the drain and the source while the gate and short are short-circuited), $I_{Dmax} = 11.5A$, $r_{DS} = 280 \, m\Omega$, $t_f = 7.5ns$, and $Q_g = 9.5 \, nC$. The transistor conduction power loss is:

$$P_{rDS} = r_{DS}I_{Srms}^2 = 0.85 \times 0.854^2 = 0.62 \, W$$

RMS current through the shunt capacitance C_1:

$$I_{C1}rms = \frac{I_I\sqrt{\pi^2 - 4}}{4} = I_I \times 0.6057 = 0.3365 \, A$$

Assume the ESR of the capacitor C_1 to be $r_{C1} = 76m\Omega$. One arrives at the conduction power loss in r_{C1}:

$$P_{rC1} = r_{C1} I_{C1rms}^2 = 0.076 \times 0.3365^2 = 0.0086 \, W$$

Assume the ESRs of the resonant inductor L and the resonant capacitor C to be $r_L = 0.5\Omega \, and \, r_C = 50m\Omega$ at $f = 3MHz$. Hence, the power losses in the resonant components are:

$$P_{rL} = \frac{r_L I_m^2}{2} = 0.5 \times \frac{1.0345^2}{2} = 0.2675 \, W$$

$$P_{rC} = \frac{r_C I_m^2}{2} = 0.05 \times 1.0345^2 = 0.0267 W$$

The drain current fall time is $t_f = 20ns$. Hence $\omega t_f = 2\pi \times 3 \times 10^6 \times 20 \times 10^{-9} = 0.377 \, rad$. The turn-off switching loss is:

$$P_{tf} = \frac{(\omega t)^2 P_O}{12} = 0.377^2 \times \frac{50}{12} = 0.59 \, W$$

The power loss (excluding the gate-drive power) is:

$$P_{LS} = P_{rLf} + P_{rDS} + P_{rC1} + P_{rL} + P_{rC} + P_{tf}$$
$$= 0.0463 + 0.62 + 0.0086 + 0.2675 + 0.0267 + 0.59 = 1.5591 \, W$$

The efficiency of the amplifier becomes:

$$\eta = \frac{P_O}{P_O + P_{LS}} = \frac{50}{50 + 1.5591} = 96.97\%$$

Assume $V_{GSm} = 8V$. One obtains the gate-drive power:

$$P_G = fV_{GSm}Q_g = 3 \times 10^6 \times 8 \times 63 \times 10^{-9} = 1.512 \, W$$

The PAE is:

$$\eta_{PAE} = \frac{(P_O - P_G)}{P_I} = \frac{P_O - P_G}{P_O + P_{LS}} = \frac{50 - 1.512}{50 + 1.5591} = 94.04\%$$

The power gain of the amplifier is:

$$k_P = \frac{P_O}{P_G} = \frac{50}{1.512} = 33.07 = 15.19 \, dB$$

The equivalent capacitance when the switch is OFF is:

$$C_{eq} = \frac{CC_1}{C + C_1} = 30.77 \, pF$$

The resonant frequencies are:

$$f_{o1} = \frac{1}{2\pi\sqrt{LC}} = 2.72 \, MHz$$

$$f_{o2} = \frac{1}{2\pi\sqrt{LC_{eq}}} = 4.38 \ MHz$$

$$f_{o2} = \frac{1}{2\pi\sqrt{LC_{eq}}}$$

Appendix: SPICE model of MOSFET

```
****************************************
*       Model Generated by MODPEX      *
*Copyright(c) Symmetry Design Systems*
*         All Rights Reserved          *
*     UNPUBLISHED LICENSED SOFTWARE    *
*    Contains Proprietary Information  *
*        Which is The Property of      *
*       SYMMETRY OR ITS LICENSORS      *
*Commercial Use or Resale Restricted  *
*    by Symmetry License Agreement     *
****************************************
* Model generated on Apr 29, 96
* Model format: SPICE3
* Symmetry POWER MOS Model (Version 1.0)
* External Node Designations
* Node 1 -> Drain
* Node 2 -> Gate
* Node 3 -> Source
M1 9 7 8 8 MM L=100u W=100u
* Default values used in MM:
* The voltage-dependent capacitances are
* not included. Other default values are:
*    RS=0 RD=0 LD=0 CBD=0 CBS=0 CGBO=0
.MODEL MM NMOS LEVEL=1 IS=1e-32
+VTO=3.84925 LAMBDA=0.00279225 KP=6.49028
+CGSO=1.18936e-05 CGDO=1e-11
RS 8 3 0.0178672
D1 3 1 MD
.MODEL MD D IS=6.51041e-09 RS=0.0106265 N=1.49911 BV=500
+IBV=0.00025 EG=1.2 XTI=3.02565 TT=1e-07
+CJO=1.08072e-09 VJ=3.67483 M=0.9 FC=0.5
RDS 3 1 2e+07
RD 9 1 0.810848
RG 2 7 3.45326
D2 4 5 MD1
* Default values used in MD1:
*    RS=0 EG=1.11 XTI=3.0 TT=0
*    BV=infinite IBV=1mA
.MODEL MD1 D IS=1e-32 N=50
+CJO=1.81945e-09 VJ=1.07167 M=0.9 FC=1e-08
D3 0 5 MD2
* Default values used in MD2:
*    EG=1.11 XTI=3.0 TT=0 CJO=0
*    BV=infinite IBV=1mA
.MODEL MD2 D IS=1e-10 N=1 RS=3e-06
RL 5 10 1
FI2 7 9 VFI2 -1
VFI2 4 0 0
EV16 10 0 9 7 1
CAP 11 10 1.81945e-09
FI1 7 9 VFI1 -1
VFI1 11 6 0
RCAP 6 10 1
D4 0 6 MD3
* Default values used in MD3:
*    EG=1.11 XTI=3.0 TT=0 CJO=0
*    RS=0 BV=infinite IBV=1mA
.MODEL MD3 D IS=1e-10 N=1
.ENDS
```